Simulating carbon and water fluxes using a coupled process-based terrestrial biosphere model and joint assimilation of leaf area index and surface soil moisture

Sinan Li [1,2], Li Zhang [1,3,*], Jingfeng Xiao [4], Rui Ma [5], Xiangjun Tian [6], Min Yan[1,3]

[1] Key Laboratory of Digital Earth Science, Aerospace Information Research Institute, Chinese Academy of Sciences, No. 9 Dengzhuang South Road, Beijing 100094, China.

[2] College of Resources and Environment, University of Chinese Academy of Sciences, No. 19A Yuquan Road, Beijing 100049, China

[3] International Research Center of Big Data for Sustainable Development Goals, Beijing 100094, China

~~Key Laboratory of Earth Observation of Hainan Province, Sanya 572029, China~~

[4]   Earth Systems Research Center, Institute for the Study of Earth, Oceans, and Space, University of New Hampshire, Durham, New Hampshire 03824, USA

[5]   School of Remote Sensing and Information Engineering, Wuhan University, Wuhan 430079, China

[6] International Center for Climate and Environment Sciences (ICCES), Institute of Atmospheric Physics, Chinese Academy of Sciences, Beijing 100029, China

* Correspondence: zhangli@aircas.ac.cn; Tel.: +86-10-8217-8193

Abstract:

Reliable modeling of carbon and water fluxes is essential for understanding the terrestrial carbon and water cycles and informing policy strategies aimed at constraining carbon emissions and improving water use efficiency. We designed an assimilation framework (LPJ-Vegetation and soil moisture Joint Assimilation, or LPJ-VSJA) to improve gross primary production (GPP) and evapotranspiration (ET) estimates globally. The integrated model, LPJ-PM (LPJ-PT-JPL$_{SM}$ Model) as the underlying model, was coupled from the Lund-Potsdam-Jena Dynamic Global Vegetation Model (LPJ-DGVM version 3.01) and a hydrology module (i.e., the updated Priestley–Taylor Jet Propulsion Laboratory model, PT-JPL$_{SM}$). Satellite-based soil moisture products derived from the Soil Moisture and Ocean Salinity (SMOS) and Soil Moisture Active and Passive (SMAP) and leaf area index (LAI) from the global Land and Ground satellite (GLASS) product were assimilated into LPJ-PM to improve GPP and ET simulations using a Proper Orthogonal Decomposition-based ensemble four-dimensional variational assimilation method (PODEn4DVar). The joint assimilation framework LPJ-VSJA achieved the best model performance (with an R^2 of 0.91and 0.81 and an ubRMSD reduced by 40.3% and 29.9% for GPP and ET, respectively, compared with those of LPJ-DGVM at the monthly scale). The GPP and ET resulting from the assimilationassimilated GPP and ET demonstrated a better performance in the arid and semi-arid regions (GPP: R^2=0.73, ubRMSD=1.05 g C m^{-2} d^{-1}; ET: R^2=0.73, ubRMSD= 0.61 mm d^{-1}) than in the humid and sub-dry humid regions (GPP: R^2=0.61, ubRMSD=1.23 g C m^{-2} d^{-1}; ET: R^2=0.66; ubRMSD=0.67 mm d$^-$

38 [1]). The ET simulated by LPJ-PM that assimilated SMAP or SMOS had a slight difference, and the SMAP

39 soil moisture data performed better than that of SMOS data. Our global simulation modeled by LPJ-VSJA

40 was compared with several global GPP and ET products (e.g., GLASS GPP, GOSIF GPP, GLDAS ET,

41 GLEAM ET) using the triple collocation (TC) method. Our products, especially ET, exhibited advantages

42 in the overall error distribution (estimated error (μ): 3.4 mm month^{-1}; estimated standard deviation of μ:

43 1.91 mm month^{-1}). Our research showed that the assimilation of multiple datasets could reduce model

44 uncertainties, while the model performance differed across regions and plant functional types. Our

45 assimilation framework (LPJ-VSJA) can improve the model simulation performance of daily GPP and

46 ET globally, especially in water-limited regions.

47 **Keywords:** Data Assimilation; SMOS; SMAP; Gross primary production (GPP); evapotranspiration

48 (ET); GLASS LAI

1. Introduction

51 Gross primary production (GPP) and evapotranspiration (ET) are essential components of the carbon

52 and water cycles. Carbon and water fluxes are inherently coupled on multiple spatial and temporal scales

53 (Law et al. 2002; Sun et al. 2019; Waring and Running 2010). Terrestrial biosphere models are the most

54 sophisticated approach for providing a relatively detailed description of such interdependent relationships

55 regarding water and carbon fluxes and understanding the response of terrestrial ecosystems to changes in

56 atmospheric CO_2 and climate (Kaminski et al. 2017). The dynamic global vegetation models (DGVMs)

are process-based dynamic terrestrial biosphere models, which can simulate water, carbon, and energy~~material~~ exchange between vegetation and the atmosphere under different conditions accounting for~~different conditions from~~ ~~the perspective of~~ vegetation physiological processes, and are widely used to estimate carbon and water fluxes of terrestrial vegetation.   However, there are still large uncertainties in carbon and water flux estimates at regional to global scales. Both diagnostic and prognostic models show substantial differences in the magnitude and spatiotemporal patterns of GPP and ET. For example, the global annual GPP estimates exhibited a large range (130–169 Pg C yr^{-1}) among 16 process-based terrestrial biosphere models (Anav et al. 2015). The global ET ranged from 70,000 to 75,000 km^3 yr^{-1}, and the uncertainty of regional or global ET estimates was up to 50% of the annual mean ET value, especially in the semi-arid regions (Miralles et al. 2016). These uncertainties mainly arise from the forcing datasets, simplification of mechanisms or imperfect assumptions in processes, and uncertain parameters in the processed models and assimilation methods (Xiao et al. 2019).

In the last two decades, remote sensing products have been assimilated into DGVMs to reduce the uncertainty in modeled carbon and water fluxes (MacBean et al. 2016; Scholze et al. (2017); Exbrayat et al. (2019)). Data assimilation (DA) is an effective approach to reduce uncertainties in terrestrial biosphere models by integrating satellite products with models to constrain related parameters or state variables. A DA system contains four main components: a set of observations, an observation operator, an underlying model, and an assimilation method. The assimilation method considers the errors from both models and observations, and reduces model uncertainties by minimizing a cost function. The Ensemble Kalman Filter (EnKF) has been widely applied in land surface process models for parameter optimization,

which significantly improve simulations by periodically updating state variables (e.g., LAI and soil moisture) using remote sensing data without altering the model structure (Rahman et al. 2021; Bonan et al. 2020; Xu et al. 2021). Yet, the EnKF relies on the instantaneous observations to update the state variable at the current time, and gives the predicted value at the next time based on the forward integration of the updated state variable. The four-dimensional variational method (4DVar) assimilation method can obtain the dynamic balance of the estimation in the time window when it is applied to the long-series forecast model (Bateni et al. 2014; and Xu et al. 2019). In particular, the Proper Orthogonal Decomposition (POD)-based ensemble 4DVAR assimilation method (referred to as PODEn4DVar) (Tian and Feng 2015) requires relatively less computation and can simultaneously assimilate the observations at different time intervals. Meanwhile, it maintains the structural information of the four-dimensional space. This method has a satisfactory performance in land DA for carbon and water variables (Tian et al. 2009; Tian et al. 2010) and can better estimate GPP and ET than EnKF (Ma et al. 2017).

Multiple sources of remote sensing data streams have been used to constrain models for assimilation. As a critical biophysical parameter of the land, leaf area index (LAI) is closely related to many land processes, such as photosynthesis, respiration, precipitation interception, ET, and surface energy exchange (Fang et al. 2019). LAI has a lot of impact onLAI is highly sensitive to the simulation of carbon and water fluxes (Liu et al. 2018), and accurate LAI estimates can improve the simulations of the carbon and water fluxes (Bonan et al. 2014;; Mu et al. 2007). He et al. (2021). assimilated land surface temperature and LAI observations into the 4DVar framework and improveds ET and GPP estimates. Soil moisture is a major driving factor affecting vegetation production in arid ecosystems, especially, in semi-

97 arid areas (Liu et al. 2020). Introducing surface soil moisture (SSM) into the model can significantly

98 improve GPP and ET simulation, particularly in water-limited areas (He et al. 2017; Li et al. 2020).

99   The advancement of earth observation, machine learning, inversion algorithms, and computer

100 technology has improved the accuracy of global LAI products and boosted model-data fusion studies

101 (Fang et al. 2019; Kganyago et al. 2020; Xiao et al. 2017). The Advanced Very High-Resolution

102 Radiometer (AVHRR) generates global LAI products with the longest historic record (since the early

103 1980s). The GLASS LAI product has been verified to have a better accuracy than that of MODIS and

104 CYCLOPES and is more temporally continuous and spatially complete (Xiao et al. 2013). Several recent

105 studies showed that the assimilation of GLASS LAI into DGVMs enhanced the performance of the

106 models in simulating carbon cycling (e.g., GPP, Net Ecosystem Exchange (NEE)) and hydrological (e.g.,

107 ET, SM) processes (Ling et al. 2019; Ma et al. 2017; Yan et al. 2016).

108   Microwave remote sensors are considered effective tools for measuring SM globally (Petropoulos et

109 al. 2015). For example, ~~surface SM~~SSM products have been derived from the Soil Moisture and Ocean

110 Salinity (SMOS) and Soil Moisture Active and Passive (SMAP) satellites equipped with an L-band

111 microwave instrument. The products from these satellites have been evaluated against in-situ observations

112 and other SSM products and overall have high accuracy(Burgin et al. 2017; Cui et al. 2018). Additionally,

113 the SMAP performs better than SMOS and other SSM products (e.g., Advanced Scatterometer (ASCAT),

114 Advanced Microwave Scanning Radiometer 2 (AMSR2)) with an overall lower error and a higher

115 correlation based on the verification with in-situ SSM data from 231 sites (Cui et al. 2018; Kim et al.

116 2018). The assimilation of SMAP data can improve the simulation accuracy of carbon and water fluxes

(He et al. 2017; Li et al. 2020) and hydrological variables (surface soil moisture, root-~~zoon~~ zone soil moisture (RZSM), and streamflow) (Blyverket et al. 2019; Koster et al. 2018; Reichle et al. 2017). In addition, the assimilation of SMAP data performed slightly better than that of SMOS and ESA CCI data (Blyverket et al. 2019).

In the nonlinear model or nonlinear observation operator, only simultaneous assimilation makes optimal use of observations (MacBean et al. 2016). Therefore, a joint assimilation of ~~soil moisture~~ SM and LAI can make full use of the two variables. From site (Albergel et al. (2010);Rüdiger et al. (2010); Wu et al.,2018) to regional assimilation (Ines et al. (2013)), many studies ~~have proposed~~showed that joint assimilation of vegetation parameters and ~~soil moisture~~SM ~~is a potential improvement in modeling~~can improve the simulation of the carbon- and water cycles. ~~For instance,. joint assimilation of soil moisture and leaf area index can improve the accuracy of crop yield estimation (Xie et al.,2018; Pan et al.,2019),~~ Over small regions and at high spatial resolution, Xie et al. (2018) and Pan et al. (2019) showed that the joint assimilation of ~~soil moisture~~SM and ~~leaf area index~~LAI ~~can~~ improved the accuracy of crop yield estimation using high-resolution satellites products from Sentinel-1 and -2. ~~with small region and high spatial resolution, which adopting observation data from stations or high-resolution satellites (e.g. Sentinel 1 and 2)~~. At a large regional scale, Bonan et al. (2020) assimilated LAI and SSM together into the Interactions between Soil, Biosphere and Atmosphere (ISBA) land model and improved the modeled GPP, ET, and runoff in the Mediterranean region. Rahman et al. (2022) jointly assimilates GLASS LAI and SMAP soil moisture to improve water and carbon flux simulations within the Noah-MP model over the Continental United States~~CONUS~~ domain. Albergel et al.(2020) jointly assimilates the ASCAT soil

moisture index (SMI) and LAI GEOV1 into ISBA ~~(Interaction between Soil Biosphere and Atmosphere)~~ ~~surface model~~ through the Global Offline Land Data assimilation system LDAS-Monde ~~LDAS Model~~ to monitor extreme events such as drought and Heatwave events. In conclusion, Kalman Filter and its variant methods are mostly used to implement~~are mostly used~~ joint assimilation methods at regional scale, which requires many kinds of observation data and their accuracy directly affects the assimilation performance.

This study stems from the researches discussed above and further explored the potential of jointly assimilating~~joint assimilating~~ satellite LAI and soil moisture products globally. Specifically, it was the first time that an updated LPJ-DGVM model was used to jointly assimilate GLASS LAI and SMAP soil moisture for simulating global water and carbon fluxes. The latest global soil moisture datasets (SMOS and SMAP) were used, and the assimilation performance of these two observations was analyzed. Since previous work showed the importance of surface soil moisture in the semi-arid and arid areas, one of the specific objectives of our study is to compare the assimilation effect in the humid and arid areas and improve the understanding of the effect of surface soil moisture on vegetation activity in wet and dry zones. In addition, compared with the assimilation methods in previous studies (mostly using Kalman Filter variants), the POD-En4DVar method is used, which greatly improves the computational efficiency.

2. LPJ-VSJA framework and assimilation strategy

2.1. Coupled- model (LPJ-PM) for assimilation

In this study, a coupled terrestrial biosphere model, LPJ-PM, was used to simulate daily GPP and ET by assimilating satellite-derived LAI and SSM. The LPJ-PM is coupled from LPJ-DGVM and PT-

156 JPL$_{SM}$. The original input data in PT-JPL$_{SM}$ were all inherited from LPJ-DGVM, with the exception of

157 relative humidity (RH) and surface soil moisture (SMOS and SMAP), including the initial LAI calculated

158 by the LPJ-DGVM or assimilated LAI obtained through the LAI assimilation scheme, canopy height, and

159 the fraction of absorbed photosynthetic effective radiation (fAPAR). The detailed processes of the LPJ-

160 PM have been described in Li et al. (2020), and the flow chart for the coupling is shown in Figure 1.

161 **Table 1. Description of the models and outputs in this study**

acronyms	Full name	Description	Output
LPJ-DGVM (Sitch et al. 2003)	Lund-Potsdam-Jena Dynamic Global Vegetation Model	This model is used as a model operator to simulated initial ET	GPP$_{LPJ}$, ET$_{LPJ}$
PT-JPL$_{SM}$ (Purdy et al. (2018))	Updated Priestley– Taylor Jet Propulsion Laboratory model	The model is used as a module of the LPJ-PM and establishes a connection between SMAP SM and ET	N/A
LPJ-PM (Li et al. (2020))	Lund-Potsdam-Jena and Updated Priestley– Taylor Jet Propulsion Laboratory coupled model	An integrated model corresponding to the coupling of~~coupled from~~ the PT-JPL$_{SM}$ and LPJ-DGVM	GPP$_{SM}$, ET$_{PM}$

	Lund-Potsdam-Jena	A process-based assimilation	GPP$_{LAI}$, ET$_{LAI}$; GPP$_{SM}$,
LPJ-VSJA (this study)	Vegetation-Soil moisture-Joint - Assimilation system	framework for assimilating LAI and SSM jointly into LPJ-PM	ET$_{SM}$; GPPjoint~~GPP$_{co}$~~; ETjoint~~ET$_{co}$~~

162

2.1.1 LPJ-DGVM

164   The LPJ-DGVM is a process-oriented dynamic model, which considers mutual interaction of carbon

165 and water cycling and is designed to simulate vegetation distribution and carbon, soil and atmosphere

166 fluxes (Sitch et al. 2003). For each plant functional type (PFT), the GPP is calculated by implementing

167 coupled photosynthesis and water balance

168   The canopy GPP is updated daily:

169
$$GPP = \frac{(J_E + J_c - \sqrt{(J_E + J_c)^2 - 4\theta J_E J_c})}{2\theta}$$
(2.1)

170 where J_C is the Rubisco limiting rate of photosynthesis, J_E is the light limiting rate of photosynthesis, and

171 the empirical parameter θ represents the common limiting effect between the two terms. J_E is related to

172 APAR (absorbed photosynthetic radiation, product of FPAR and PAR), while J_C is related to Vcmax

173 (canopy maximum carboxylation capacity, μ mol $CO^2/m^2/s$):

174
$$J_E = C_1 APAR$$
(2.2)

175
$$J_C = C_2 V_{C\,max}$$
(2.3)

176   where C_1 and C_2 are determined by a variety of photosynthetic parameters and the intercellular partial

177   pressure of CO_2, which is related to atmospheric CO_2 content and further altered by leaf stomatal

178   conductance (Sitch et al. 2003). APAR and FPAR are directly related to LAI.

179   In the water cycle module, ET is calculated as the minimum of a plant- and soil-limited supply

180   function (E_{supply}) and the atmospheric demand (E_{demand}) (Haxeltine and Prentice 1996; Sitch et al.

181   2003).The soil structure is simplified to a "two-layer bucket" model (the top soil layer at a 0-50 cm depth

182   and the bottom layer at a 50-100 cm depth) .

183
$$E_S = Ep \times Wr_{20} \times (1 - fv) \qquad (2.4)$$

184   In this module, it is assumed that the soil layer above 20 cm produces water through evaporation,

185   and Wr_{20} is the relative water content of the soil above 20 cm, which is used as the only soil water limit

186   for calculating vegetation transpiration and soil evaporation. In the evapotranspiration estimation, the

187   over-simplification of soil structure and soil water limitation lead to a large error (Sitch et al. 2003), while

188   LPJ-DGVM cannot directly assimilate surface soil water due to the limitation of soil layer stratification

189   , and therefore, the satellite-derived ~~surface SM~~SSM cannot be assimilated into LPJ-DGVM directly. The

190   oversimplified soil structure and single soil moisture limitation inevitably lead to sizeable uncertainty in

191   ET simulation. Additionally, the monthly input caused a daily variation of the modeled SM, which was

192   also not transmitted to the calculation of GPP and ET. Thus, the updated PT-JPL model (hereafter referred

193   to as PT-JPL$_{SM}$) was coupled with LPJ-DGVM and the model structure was modified so that ~~surface~~

194   ~~SM~~SSM can be directly assimilated into the coupled model at the daily time step.

195   2.1.2 PT-JPL$_{SM}$

196   In PT-JPL$_{SM}$, three ET components are modelled: soil evaporation (E), vegetation transpiration (T),

197   and leaf evaporation (I). The PT-JPL$_{SM}$ introduced a constraint (0–1, C$_{RSM}$) of ~~surface~~ SSM for T and E,

198   which was used to avoid the implicit soil water control (represented by f$_{SM}$=RH^{VPD}) in the PT-JPL model.

199   Vegetation transpiration:

200
$$C_{RSM} = (1 - RH^{4(1-VWC)(1-RH)})C_{SM} + (RH^{4(1-VWC)(1-RH)})C_{TRSM}$$

201
$$C_{RSM} = (1 - RH^{4(1-VWC)(1-RH)})C_{SM} + (RH^{4(1-VWC)(1-RH)})C_{TRSM}$$
(2.5)

202
$$C_{TRSM} = 1 - (\frac{w_{CR}-w_{obs}}{w_{CR}-w_{pwp\_CH}})^{\sqrt{CH}} \qquad C_{TRSM} = 1 - (\frac{w_{CR} - w_{obs}}{w_{CR} - w_{pwp\_CH}})^{\sqrt{CH}}$$,

203   (2.6)

204   where w$_{obs}$ is the SMAP SSM, w$_{pwp}$ is the water content at the wilting point, and ~~w$_{fc}$~~ VWC is ~~the~~

205   volumetric water content~~water content at field capacity, which is determined by the properties of the soil~~.

206   W$_{CR}$ is a crucial parameter in characterizing the extent of SM restriction on ET; w$_{pwp\_CH}$ is the canopy

207   height (CH) adjusted surface soil moisture wilting point and is related to the potential of roots capturing

208   water from deeper sources to limit the transpiration rate and characterize the SM availability (Purdy et al.,

209   2018; Evensen 2003; Serraj et al., 1999). The specific formula is given in Purdy et al. (2018).

210   Soil evaporation:

$$C_{RSM} = \frac{w_{obs} - w_{pwp}}{w_{fc} - w_{pwp}}$$

211 (2.7)

212   The proportion of available water limits the soil evapotranspiration to the maximum available water.

213 This scalar was formulated to represent the relatively accurate extractable water content for the vegetation,

214 determined by soil properties and the water available for evaporation, which is estimated via surface water

215 constraints.

216   The SMAP ~~S~~SM ~~as surface SM data~~ was applied to model global ET using PT-JPL$_{SM}$ and the results

217 demonstrated the largest improvements for ET estimates in dry regions (Purdy et al. 2018). Due to the

218 limitation of soil stratification in LPJ-DGVM, the model was coupled with an updated remote-sensing

219 ET algorithm in the PT-JPL$_{SM}$ that could better simulate ET in water-limited regions than in humid regions

220 (Purdy et al. 2018).

221 *2.2. Assimilation scheme and experiment procedure*

222   To improve the prediction capability of LPJ-PM, we designed three assimilation schemes:

223 assimilating LAI ~~only~~only (~~scheme 1~~LAI-only, **output: ET$_{LAI}$, GPP$_{LAI}$**), assimilating SSM only (SSM-

224 only~~scheme 2~~, **output: GPP$_{SM}$, ET$_{SM}$**), and joint assimilation of LAI and SSM (Joint LAI and SSM

225 assimilation~~scheme 3~~, **output: ET$_{joint}$~~co~~, ~~GPP$_{co}$~~GPP$_{joint}$**), i.e., LPJ-VSJA framework) to test the

226 assimilation performance for simulating GPP and ET.

227   The proposed LPJ-VSJA framework consists of four main components: the model operator (the LPJ-

228   PM), the observation operator (to establish the relation between the assimilation variable and the observed

229   variable), the observation series (GLASS LAI and SMOS or SMAP products), and the assimilation

230   algorithm (POD4DVar). With the surface soil moisture constraint in the PT-JPL$_{SM}$, the LPJ-VSJA

231   corrects the output fluxes (GPP and ET in this study).
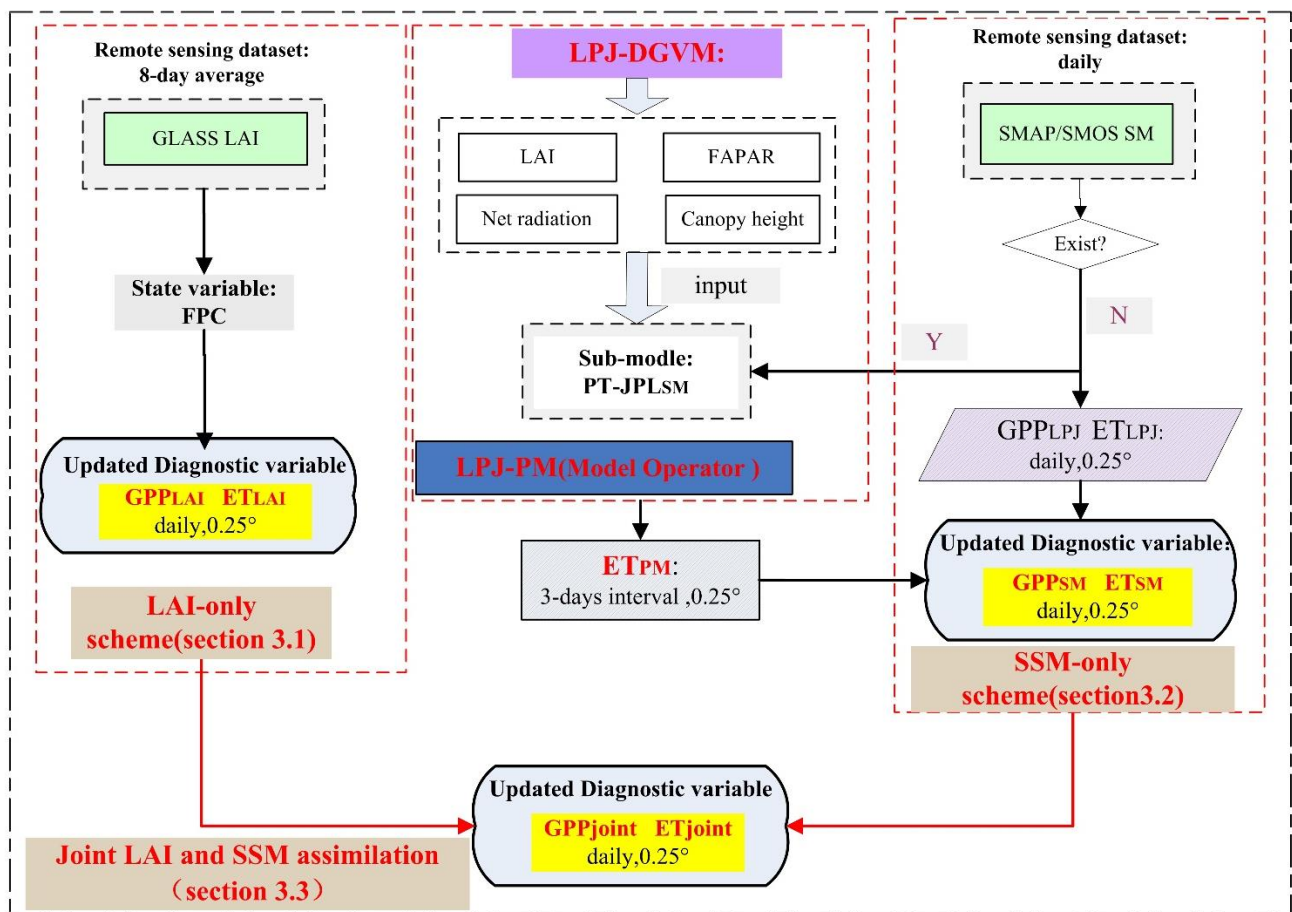
232

233   **Figure 1. Flowchart of the LPJ-VSJA assimilation scheme: three assimilation schemes and the coupled**

234   **model: LPJ-PM. (adapted from Li et al., 2020). The abbreviation of model and assimilation framework is**

235   **explained in Table 1.**

236

237   The experiment consisted of six steps:

238   Step 1: initialize the LPJ-DGVM and output the reference state variables without assimilation over

239   the experimental period (2010–2018), referred to as the "Control run" scenario.

240   Step 2: implement ~~schemes 1, 2, and 3,~~ three assimilation schemes respectively, and the results

241   represent the assimilation integration state (daily GPP and ET assimilation results are referred to as the

242   "GPP$_{LAI}$" and "ET$_{LAI}$" in ~~scheme 1~~ LAI-only scheme ;"GPP$_{SM}$" and "ET$_{SM}$" in SSM-only scheme ~~scheme~~

243   ~~2~~ and "GPP$_{joint}$ ~~GPP$_{co}$~~" and "ET$_{joint}$ ~~ET$_{co}$~~" in Joint LAI and SSM assimilation scheme ~~scheme 3~~. This

244   scenario used the same input data and model parameter scheme with the "Control run" scenario.

245   Step 3:evaluate GPP and ET results (three schemes ~~1, 2 and 3~~) by comparing the parameters, R^2

246   (correlation coefficient), BIAS, and ubRMSD (unbiased root mean square deviation), for conditions of

247   without-DA ("Control run" scenario) and with-DA states, and assess the assimilation performance of

248   separate assimilation ~~(schemes 1 and 2)~~ and joint assimilation ~~(scheme 3)~~ to determine the optimal

249   assimilation scheme for GPP and ET, respectively.

250   Step 4:   evaluate the in-situ GPP and ET resulting from the assimilation ~~assimilated GPP and ET~~

251   ~~results~~ where the sites are located in wet or dry regions by dividing these validation sites into four parts

252 (humid, sub-dry humid, semi-arid, and arid regions), and this step was designed to assess the superiority

253 of the proposed assimilation scheme in water-limited areas.

254 Step 5: compare the ET assimilation performance by assimilating the SMOS data with that by

255 assimilating the SMAP data.

256 Step 6: evaluate the simulated GPP and ET maps based on the optimal assimilation scheme against

257 existing global flux products.

258 2.2.1 LAI-only assimilation scheme~~DA scheme 1: LAI assimilation~~

259 In~~ ~~ the LAI-only assimilation scheme~~assimilation scheme 1~~, the observation operator determines

260 the relationship between LAI and foliage projective cover (FPC) in the process model (equation 2.1), and

261 the assimilated LAI will be propagated by energy transmission and ecosystem processes (e.g.

262 photosynthesis, transpiration of vegetative process) in the dynamic model to improve GPP and ET

263 simulations (Bonan et al. 2014; Mu et al. 2007). FPC, the vertically projected percentage of the land

264 covered by foliage, regulates the rate of photosynthate conversion and transpiration. In this study, the

265 GLASS LAI with 8-day interval for the period 2010–2018 was selected as the observation dataset for

266 assimilation, and the FPC state variable was updated daily through running the LPJ-PM (FPC_{DA}, GPP_{LAI},

267 ET_{LAI} in this study) as shown below:

268 $$FPC = 1 - e^{-0.5LAI} \qquad (2.1)$$

269   We set the model and observation errors at a given time as 20% and 10% (scale factor) of the LAI

270   value and the observed LAI value, respectively. By verifying the assimilation performance (R^2, RMSD,

271   BIAS) for different scale factors(f) of model simulation and observations in the range of 0.05 to 0.40,

272   taking a step size of 0.05 (a total of 64 combinations), the optimal scale factors (0.2 and 0.1) were

273   determined (Bonan et al., 2020).The model and observation errors was the LAI value multiplied~~y~~ by f.

274   The model integration generation method described by Pipunic et al. (2008) was used to determine the

275   minimum number of ensemble members required to achieve maximum efficiency, and the number of sets

276   was 20.

277   2.2.2 SSM-only assimilation scheme~~DA scheme 2: SSM assimilation~~

278   In this scheme, the ~~surface~~ SSM products (SMOS or SMAP) were assimilated into LPJ-PM to

279   obtain more accurate ET (ET_{SM}) estimates in water-limited areas. The observation series was the SMOS

280   or SMAP SSM product, and the observation operator was the PT-JPL$_{SM}$ model. The ET_{PM} (see Table 1)

281   was estimated by the coupled model (LPJ-PM) introducing ~~surface~~ SSM ~~was directly assimilated~~ as a

282   diagnostic variable. The ET values resulting from the assimilation~~assimilated ET~~ was applied to compute

283   the top layer SM (50 cm) at the next time step (a nonlinear soil water availability function described by

284   Zhao et al. (2013), providing feedback for subsequent hydrologic and carbon cycle processes. Then, the

285   updated SM values regulated the GPP simulation (output: GPP_{SM}). Different from other "constant" ET

286   observations, the ET_{PM} ("observation") at each time t were adjusted by absorbing intermediate variables

287   updated after assimilation at time t-1. The ET_{PM} was shown to be better than ET simulated by LPJ-DGVM

288   but not as good as that simulated by the model with SMAP SSM assimilated (Li et al. 2020). Thus, it is

289   also proven that this SSM assimilation schemes could improve the accuracy of ET simulations (Li et al.

290   2020).

291   All assimilation simulations were conducted between January 2010 and December 2018. Between

292   January 2010 and April 2015, SMOS data were used for assimilation; and after May 2015, both SMOS

293   and SMAP data were used for assimilation. An assimilation scheme was conducted when RH and SMOS

294   or SMAP SSM data existed simultaneously; otherwise, the original simulation of the LPJ-DGVM was

295   conducted directly without adjustment of assimilation.

296   Similar to the LAI assimilation scheme, the model and observation errors were set as 15% and 5%

297   of ET_{LPJ} and ET_{PM}, respectively (LPJ-PM was adopted before assimilation). The number of ensemble

298   members was set to 50.The ET_{PM} must be rescaled to the ET_{LPJ} distribution via their corresponding

299   cumulative probabilities using the cumulative distribution function (CDF) matching to avoid introducing

300   any ~~bias~~ BIAS in the LPJ-VSJA system (Li et al. 2020).

301   2.2.3 Joint LAI and SSM assimilation scheme ~~DA scheme 3: joint assimilation of LAI and SSM~~

302   In this scheme, both LAI from GLASS and SSM from SMOS or SMAP were the observation datasets.

303   The GLASS LAI was assimilated ~~by scheme 1~~ to obtain the FPC_{DA} and ET_{LAI}, and then the FPC_{DA} served

304   as input to LPJ-PM to simulate optimized ET_{PM}, and the ET_{joint} was generated using ET_{LAI} and ~~was~~

305   ~~further assimilated with ET_{PM} to generate~~ ET_{PM}~~co~~. Then, the SM (referred to as SM_{CO} in Figure S1)

306   updated by ~~ET~~joint~~ETjointETCO~~ and the FPC_{DA} were used as input to correct GPP

307   (~~ET~~joint~~GPPjointGPP~~co).

308   Here, we applied the error regulation in the LAI-only scheme ~~scheme 1~~ and maintained the error

309   setting of the LAI observation and model simulation. Considering the transmission of integrated model

310   error, we recalculated the model error of LPJ-PM after the LAI assimilation and set model and observation

311   errors of ET_{LAI} and ET_{PM} to be 15 and 10%, respectively.

2.3. POD-Based Ensemble 4D Variational Assimilation Method

313   The Proper Orthogonal Decomposition (POD)-based ensemble four-dimensional variational (4DVar)

314   assimilation method (referred to as PODEn4DVar) (Tian and Feng 2015) has the advantage of avoiding

315   the calculation of adjoint patterns as its incremental analysis field, which can be represented linearly by

316   the POD base (Transformed OP (Observing Perturbation) and MP (Model Perturbation)). Moreover, the

317   PODEn4DVar can simultaneously assimilate multiple-time observation data and provide flow-dependent

318   (the flow-dependent is the ensembles of forecasting statistical characteristics in the t time) error estimates

319   of the background errors. It has shown advantages in terrestrial assimilation, Tan-Tracker system ~~joint~~

320   ~~DA~~(a Chinese carbon cycle data-assimilation system;~~,~~ in Chinese, "Tan"~~m~~ means carbon), and Radar

321   assimilation (Tian et al. 2010; Tian et al. 2009; Tian et al. 2014; Zhang and Weng 2015).

322   By minimizing the following initial incremental format of the cost function in the 4DVar algorithm,

323   an analysis field can be obtained:

$$J(x') = \frac{1}{2}(x')B^{-1}(x') + \frac{1}{2}[y'(x') - y'_{obs}]^T R^{-1}[y'(x') - y'_{obs}]$$

324

Here, the $x' = x - x_b$, $y'(x') = y(x' + x_b) - y(x_b)$, $y'_{obs} = y_{obs} - y(x_b)$, $y = H[M_{to \to tk}(x)]$.

326 $x'(x'_1, x'_2, \ldots, x'_N)$ is the model perturbation (MP) matrix and $y'(y'_1, y'_2, \ldots, y'_N)$ is the

327 observation perturbation (OP) matrix with N samples. Following Rüdiger et al. (2010), the LAI

328 perturbation was set to a fraction (0.001) of the LAI itself. The perturbation of ET_{PM} and ET_{LPJ} conforms

329 to a Gaussian distribution with a mean of 0 and a specified covariance (10 and 5% of the ET_{PM} and ET_{LPJ}

330 at time t). The subscript b represents the background field, the superscript T represents a transpose, H is

331 the observation operator of the ~~scheme 1~~LAI-only assimilation ~~scheme~~scheme as described in section

332 2.2.1, and the ~~scheme 2~~SSM-only assimilation scheme is the PT-JPL$_{SM}$ (described in 2.1.2). M is the

333 forecast model (LPJ-PM in this study), B is the background error covariance, R is the observation error

334 covariance, and obs denotes observation.

335 Assuming the approximately linear relationship between OP(y') and MP(x'), POD decomposition

336 and transformation were successively conducted for OP and MP. The transformed OP samples ($\Phi_y =$

337 $y'_1, y'_2, \ldots, y'_n$) are orthogonal and independent, and the transformed MP samples ($\Phi_x =$

338 $x'_1, x'_2, \ldots, x'_n$) are orthogonal to the corresponding OP samples, where n is the number of POD modes.

339 The manifestation of the background error covariance is the same as the Ensemble Kalman filter

340 (EnKF, Evensen (2004)), and the incremental analysis x'_a was expressed by the $\Phi_{x,n}$, and $\widetilde{\Phi}_y(\widetilde{\Phi}_y =$

341 $[(n-1)I_{n \times n} + \Phi_{y,n}^T R^{-1} \Phi_{y,n}]^{-1} \Phi_{y,n}^T R^{-1}$). Finally, the optimal analysis x_a is calculated as $x_a = x_b +$

342    $\Phi_{x,n}\widetilde{\Phi}_y y'_{obs}$. The detailed derivation process of the algorithm is described by a previous study (Tian et

343   al. 2011).

344   In the ensemble-based method (Evensen et al.,2004), the number of ensemble members is usually

345   fewer than that of the observation data and the degrees of freedom of the model variables, and spurious

346   long-range correlations occur between observation locations and model variables. A practical method, the

347   localization technique, is applied to address this issue (Mitchell et al. 2002). The final incremental analysis

348   is rewritten as:

349
$$x'_a = \Phi_{x,n}\widetilde{\Phi}_y y'_{obs} C_0\left(\frac{d_h}{d_{h,0}}\right) \cdot C_0\left(\frac{d_v}{d_{v,0}}\right)$$

350   where d_h and d_v are the horizontal and vertical distances between the spatial positions of state and

351   observed variables, respectively; and $d_{h,0}$ and $d_{v,0}$ are the horizontal and vertical covariance localization

352   Schur radii, respectively. The filtering function C_0 is expressed as:

353
$$C_0(r) = \begin{cases} -\frac{1}{4}r^5 + \frac{1}{2}r^4 + \frac{5}{8}r^3 - \frac{5}{3}r^2 + 1, & 0 \le r \le 1, \\ \frac{1}{12}r^5 - \frac{1}{2}r^4 + \frac{5}{8}r^3 + \frac{5}{3}r^2 - 5r + 4 - \frac{2}{3}r^{-1}, & 1 \le r \le 2, \\ 0, & 2 < r \end{cases}$$

354   where r is the radius of the filter.

355   The assimilation algorithm is mainly divided into two steps: (1) prediction: run LPJ-PM in the

356   current assimilation window and generate simulation results and background field vectors; (2) update: the

357   algorithm is used to calculate the optimal assimilation increment x'_a and analysis solution x_a, and the

358 simulation results and the initial conditions of the model in the current window are updated using the

359 analysis solution. The updated initial conditions were applied for model LPJ-PM prediction, and the above

360 process was repeated.

361 *2.4. Validation method for assimilation performance*

362 The R^2 (~~correlation coefficient~~~~squared correlation coefficient~~coefficient of determination),

363 ~~Bias~~BIAS, and ubRMSD (unbiased root mean square deviation) between simulation and tower-based

364 observations were applied for evaluation. In addition, a Taylor chart was also used to demonstrate the

365 performance of two ET estimations with different SSM observations in terms of R, ubRMSD, and

366 Normalized Standard Deviation (NSD) on 2D plots, to display how closely the datasets matched

367 observations in one diagram (Taylor 2001). In the Taylor diagram, NSD represents the radial distance

368 from the origin point and the correlation with the site observations as an angle in the polar plot. The

369 ubRMSD is the distance between the observation and the model and is represented in the ~~figure~~ Taylor

370 chart as a green semi-circular arc with point A as the center of the circle. The closer the model point to

371 the reference point (Point A), the better the performance. This diagram is convenient and visual in

372 evaluating multiple aspects of various models.

373 The error variance of GPP and ET products was estimated using the triple collocation (TC) approach

374 (Stoffelen 1998) to validate the global simulation in this study. The method has been extensively applied

375 in the study of hydrology and oceanography (Caires and Sterl 2003; Khan et al. 2018; O'Carroll et al.

376 2008; Stoffelen 1998), particularly in SM studies (Chan et al. 2016; Kim et al. 2018). The TC provides a

377 reliable platform for comparison of spatial assimilation results and in-situ measurements. In this

378 experiment, no calculation was performed on the non-vegetated areas where the correlation was lower

379 than 0.2 to have independent datasets and avoid correlated errors (crucial assumptions in TC) (Yilmaz

380 and Crow 2014).

381   In this study, the five products were divided into three product categories, including satellite product

382 (MODIS, GOSIF GPP), reanalysis product (GLASS, GLDAS) and data assimilation product (GLEAM

383 ET, LPJ-VSJA) (Li et al.,2018). One product in each category was selected to form a group to calculate

384 their error. The LPJ-VSJA product was set as the reference data.

385   For GPP products, GOSIF, GLASS, and LPJ-VSJA were treated as a group, and MODIS, GLASS

386 and LPJ-VSJA were treated as another group to calculate the errors; the final errors were determined by

387 the average of these two.

388   Similarly, to calculate the errors for ET, GLEAM, GLASS, and MODIS were chosen as a group;

389 LPJ-VSJA, GLDAS, and MODIS were treated as a group; LPJ-VSJA, GLASS and MODIS were

390 considered as a group. In order to reduce the influence of orthogonality hypothesis of error, the first and

391 third groups are for indirect and effective comparison between LPJ-VSJA product and GLEAM product.

392 **3.   Experiment sites and data**

393 *3.1. Description of flux tower sites*

394   We   screened   over   300   EC   flux   sites   across   the   globe   from   the   FLUXNET2015

395 (https://fluxnet.fluxdata.org/data/fluxnet2015-dataset/),   AmeriFlux   (http://public.ornl.gov/ameriflux),

and the HeiHe river basin (Liu et al. (2018), http://www.heihedata.org)) for the evaluation of assimilation performance over the period from January 2010 to December 2018. The in-situ half-hourly LE and GPP data from the sites were aggregated into daily data. The daily gap-filled data were excluded if the percentage of gap-filled half-hourly values was more than 20%. Then we corrected the data of energy non-closure by using the Bowen ratio closure method (Twine et al. 2000) to improve the energy closure rate (Huang et al. 2015; Yang et al. 2020). The data were selected to cover the 2010–2018 period with at least one year of reliable data, and the result from the error of assimilation is relative to the LE value and seasonal variation (Purdy et al. 2018; Zou et al. 2017). It is essential to have available data every month during a one-year period, and only days with less than 25% missing data were processed per month (Feng et al. 2015). In addition, for flux tower data, the data were also excluded for the analysis if the SMAP/SMOS SSM data were not of good quality.

Finally, we identified a total of 105 sites across the globe encompassing five major biomes: grassland (18 for GPP and 19 for ET), savanna (11), shrubland (4), forest (49 and 53), and cropland (13 and 14). In the comparative analysis of the performance for simulating ET by assimilating SMOS and SMAP SSM data separately, we selected 46 AmeriFlux sites (Figure S3) with at least one year of reliable data from 2015 to 2018 based on the simultaneous availability of SMAP and SMOS data, including grassland (19), savanna (11), shrubland (5), forest (23), and cropland (7). Figure S2 and S3 illustrate the location and distribution of the 105 and 46 EC flux tower sites, respectively. A more detailed description is summarized in the Supporting Information Table S1.

3.2. Remote sensing datasets: LAI and SSM

The GLASS LAI product with an 8-day time step (8-day average) and 5 km resolution was derived from MODIS and CYCLOPES surface reflectance and ground observations using general regression neural networks (GRNNs) (~~Liang et al. 2013; Xiao et al. 2016~~Xiao et al. 2013; Xiao et al. 2016). The verification of the product using the mean values of high-resolution LAI maps showed that the GLASS LAI values were closer to these high-resolution LAI maps (RMSD= 0.78 and R^2= 0.81) (~~-~~Xiao et al. 2016; Liang et al. 2013). Therefore, the GLASS LAI product has satisfactory performance and can be assimilated into terrestrial biosphere models.

The SMAP mission (Entekhabi et al. 2010) and SMOS mission (Jacquette et al. 2010), the two dedicated soil moisture satellites currently in orbit equipped with L-band microwave instruments, provide ~~surface~~ SSM retrievals. We chose the SMOS-L2 product and the SMAP-L3-Enhanced product, which both provide global coverage every three days for soil depth of 5 cm. Only good-quality SMAP and SMOS data were used. The grid cells with water areas larger than 10% and those with less than 50% good-quality data in one year were masked out, which alleviates the undesirable model simulations caused by the decrease in SMAP retrieval accuracy (Chan et al. 2016; O'Neill et al. 2010). We only adopted the data with an uncertainty below 0.1 m^3 m^{-3}, in the actual range (0.00–0.6 m^3 m^{-3}), and the temperature of the LSM observation layer (the second layer) was higher than 2 °C (Blyverket et al. 2019).

432   ~~Both t~~The GLASS LAI, SMOS and SMAP observations ~~was~~ were resampled to 9 km for site

433   simulation and 0.25° for ~~spatial~~ regional simulation. The 8- day average of GLASS LAI were assimilated

434   for each day, and the SMAP or SMOS SSM was assimilated every 3 days.

3.3. Model-forcing and validation datasets

436   In this study, the meteorological, soil property, and CO_2 concentration datasets were used to drive

437   the LPJ-PM. The climate-driven ~~dataset~~datasets used for the initialization of the LPJ-DGVM are the

438   ~~A~~atmospheric CO_2~~CO2~~ concentrations (1901-2018) of i~~I~~ce-core measurements and atmospheric

439   observations at the Mauna Loa Observatory and CRU TS4.03 version Climate data from 1901 to 1930

440   provided by the Climatic Research Unit (CRU) of the Climate Laboratory, University of East Anglia, UK,

441   including monthly precipitation, surface temperature, cloud cover and wet day. In the simulation period

442   of 2010-2018, the Modern Era Retrospective-Analysis for Research and Applications Version 2

443   (MERRA-2) was ~~used~~adopted, and the variables used includ~~ing~~ed precipitation, temperature, cloud cover

444   and relative humidity. Soil properties (including limited water content of vegetation at wilting points,

445   field capacity and Soil porosity) from Harmonized World Soil Database (HWSD) V1.2 dataset (Wieder

446   et al. 2014) were selected as inputs to the PT-JPLSM model. Table 2 provides the spatial and temporal

447   characteristics of the model-forcing datasets in the LPJ-PM (submodule: LPJ-DGVM and PT-JPL$_{SM}$).

448   The GLASS LAI product, SMOS-L2 product and the SMAP-L3-Enhanced product were assimilated

449   to ~~produce~~simulate GPP and ET.For site simulation, in order to maintain consistency with the SMAP

450   Enhanced 3 Level product (Entekhabi et al. 2010), model-forcing data were resampled to a 9 km spatial

451 resolution based on EASE-2 projection grid. In the global spatial simulation, the model-forcing datasets

452 were resampled~~were interpolated~~ to 0.25° based on the bilinear method to ensure the consistency of spatial

453 representation. ~~Table 2 provides the spatial and temporal characteristics of the model-forcing datasets in~~

454 ~~the LPJ-PM (submodule: LPJ-DGVM and PT-JPL~~SM~~).~~

455

456 **Table 2. List of the selected forcing and remote-sensing datasets used in this study**

Datasets	Variable	Period	Spatial resolution	References
CRU TS v4.1[a]	Cloud cover, temperature, precipitation, wet day	1901-1930	0.5°× 0.5°	New et al. (2000), https://cruda ta.uea.ac.uk/c ru/data/hrg/
Ice-core measurements and atmospheric observations at the Mauna Loa Observatory [a]	Atmospheric CO_2 concentrations	1901-2018	NA	(Etheridge et al. (1996); Keeling et al. (1995)) , https://scrippsc o2.ucsd.edu/da ta/atmospheric

_co2/

MERRA-2 [a]	Precipitation, surface temperature, cloud fraction, relative humidity	2010-2018	0.5°× 0.625°	Rienecker et al. (2011) (https://www.esrl.noaa.gov/psd/)
HWSD (v121)[b]	Soil texture data	NA	1 km×1 km	Wieder et al. (2014) (http://daac.ornl.gov)
SPL3SMP_E[b]	Surface soil moisture	2015.4–present	9 km×9 km	Entekhabi et al. (2010), (https://smap.jpl.nasa.gov/)
GLASS LAI [a,b]	Leaf area index	2010-2018	5 km×5 km	Xiao et al. (2016), (http://www.glass.umd.edu/Download.

					html)
					Jacquette et al.
					(2010),(https:
					//earth.esa.int
SMOS_L3 CATDS[b]	Surface soil moisture	2010-present	25km×25 km		/eogateway/
					missions/smo
					s)

[a]: forcing dataset for LPJ-DGVM

[b]: external input dataset for PT-JPL$_{SM}$

We used four global ET products and three global GPP products (Li et al. 2018; Li and Xiao 2019; Wang et al. 2017) that was resample to 0.25° to evaluate the performance of the model with the joint assimilation scheme. Table 3 shows the details of these GPP and ET products.

Table 3. Global GPP and ET products for comparison in this study

Product	Dataset	Temporal resolution	Spatial resolution	Retrieval algorithm	References

MOD17A2	GPP and ET	8-day average	1 km × 1 km	GPP: Based on the light use efficiency (LUE) model ET: Improved Penman formula	Running et al. (2004)
GLASS	GPP and ET	8-day average	5 km × 5 km	GPP: EC-LUE model ET: Combining five Bayesian averages based on process models (BMA)	Yuan et al. (2010)
GOSIF GPP	GPP	8-day average	0.05° × 0.05°	Estimated from solar-induced chlorophyll fluorescence with GPP-SIF relationships	Li and Xiao (2019)
GLDAS ET	ET	daily	0.25°× 0.25°	Processed model assimilation	Fang et al. (2009)
GLEAM v3a ET	ET	daily	0.25°× 0.25°	Processed model assimilation	Martens et al. (2017)

464

465 **4. Results**

4.1. Performance of LPJ-PM for simulating GPP and ET with the assimilation of LAI and soil moisture

4.1.1 Accuracy assessment of GPP for separate and joint assimilation

In general, the R^2 between GPP_{LPJ} and GPP_{OBS} was above 0.4 at most of the sites (62 sites) and were relatively weak for some sites. The LAI assimilation improved the simulations at most sites (R^2 value increased at 82 sites), particularly for sites in the U.S. and Europe (Figure ~~S2~~S4). The R^2 improvement from the LAI assimilation (~~scheme 1~~LAI-only assimilation) was superior to that from the SSM assimilation (Figure S4~~2 R²~~ (b) and (c)). The performance of the joint assimilation ~~(scheme 3)~~ was similar to that of ~~scheme 1~~LAI-only assimilation~~-~~. Sites (Figure S5~~2 BIAS~~ (a)) showed positive BIAS~~bias~~ (GPP_{OBS}-GPP_{LPJ}) were mainly distributed in the humid and sub-dry~~dry-sub~~ humid forest, grassland, and arid cropland regions, showing an underestimation for GPP_{OBS}. The assimilation improved the accuracy for overestimated sites, but there was no significant improvement for underestimated sites. The ubRMSD implied that the SSM assimilation alone had a better performance than the LAI assimilation alone, especially for sites in arid areas(Figure 2). The analysis of the above three statistical measures (R^2, BIAS, and ubRMSD) indicated that the accuracy of joint assimilation was much better than that of separate assimilation.

At the seasonal scale, all three assimilation schemes corrected the model trajectory and significantly improved the growing season simulations, especially for peak values (IT-Tor, US-NR1, US-NE1) (Figure 3). In addition, the linear fitting of GPP_{joint}~~GPPco GPPJOINT~~ and GPP_{OBS} on a monthly scale was closer to 1:1 (y= 0.92x + 21.66 p < 0.001) than that of GPP_{LAI} (y= 0.89x + 28.3, p <

485   0.001) and GPP~SM~ (y= 0.86x + 41.70, p < 0.001) (Figure ~~S5~~S9). The results in Table S2 support the

486   above analysis, and the joint assimilation showed advantages in overall accuracy in both arid and humid

487   areas.
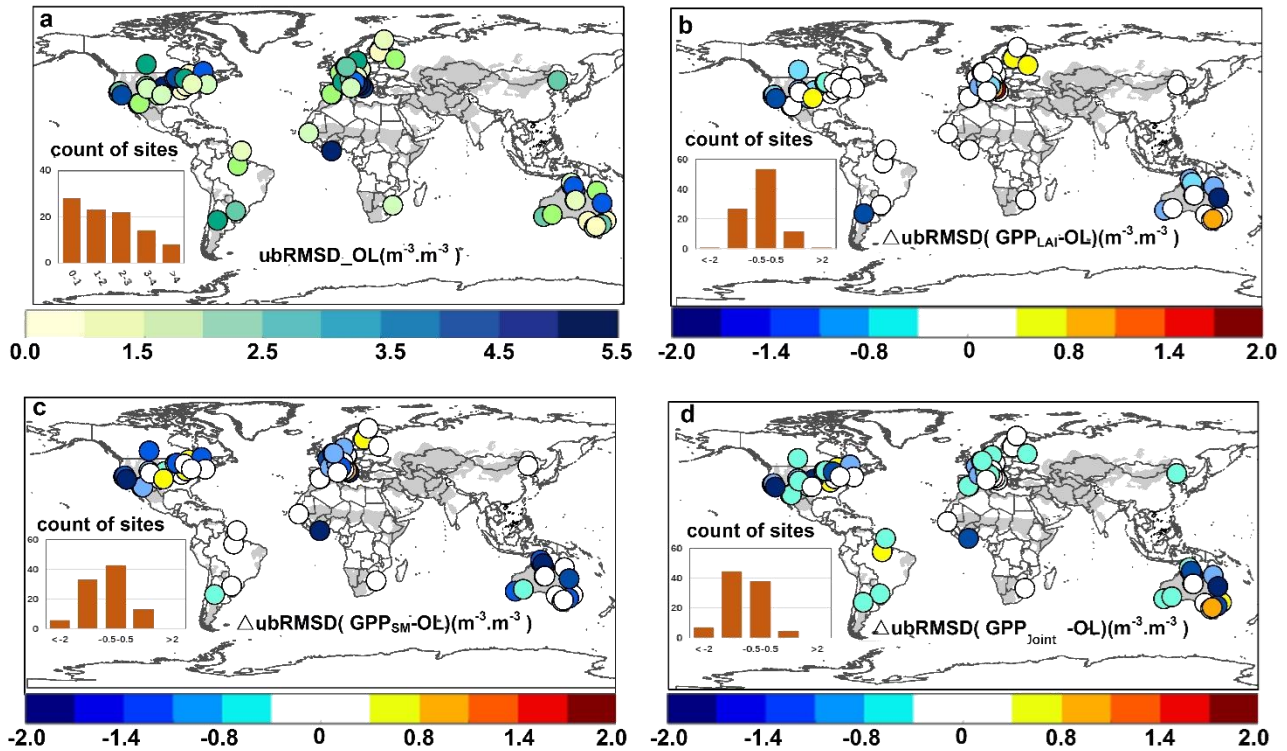
488

Figure 2   **(a)The Unbiased Root Mean Square Error (~~ubRMSE~~ubRMSD) between the ~~GPP(~~GPP~LPJ~~~)~~ ~~simulated~~**

~~by the LPJ-DGVM~~ and the site observations, the yellow/blue indicating low/high ~~correlation~~ ubRMSD; (b)△ubRMSD

(GPP~LAI~- GPP~LPJ~);(c)△ubRMSD(GPP~SM~- GPP~LPJ~); (d)△ubRMSD(GPP~Joint~~~co~~- GPP~LPJ~), blue/red represent

positive/negative values.

489
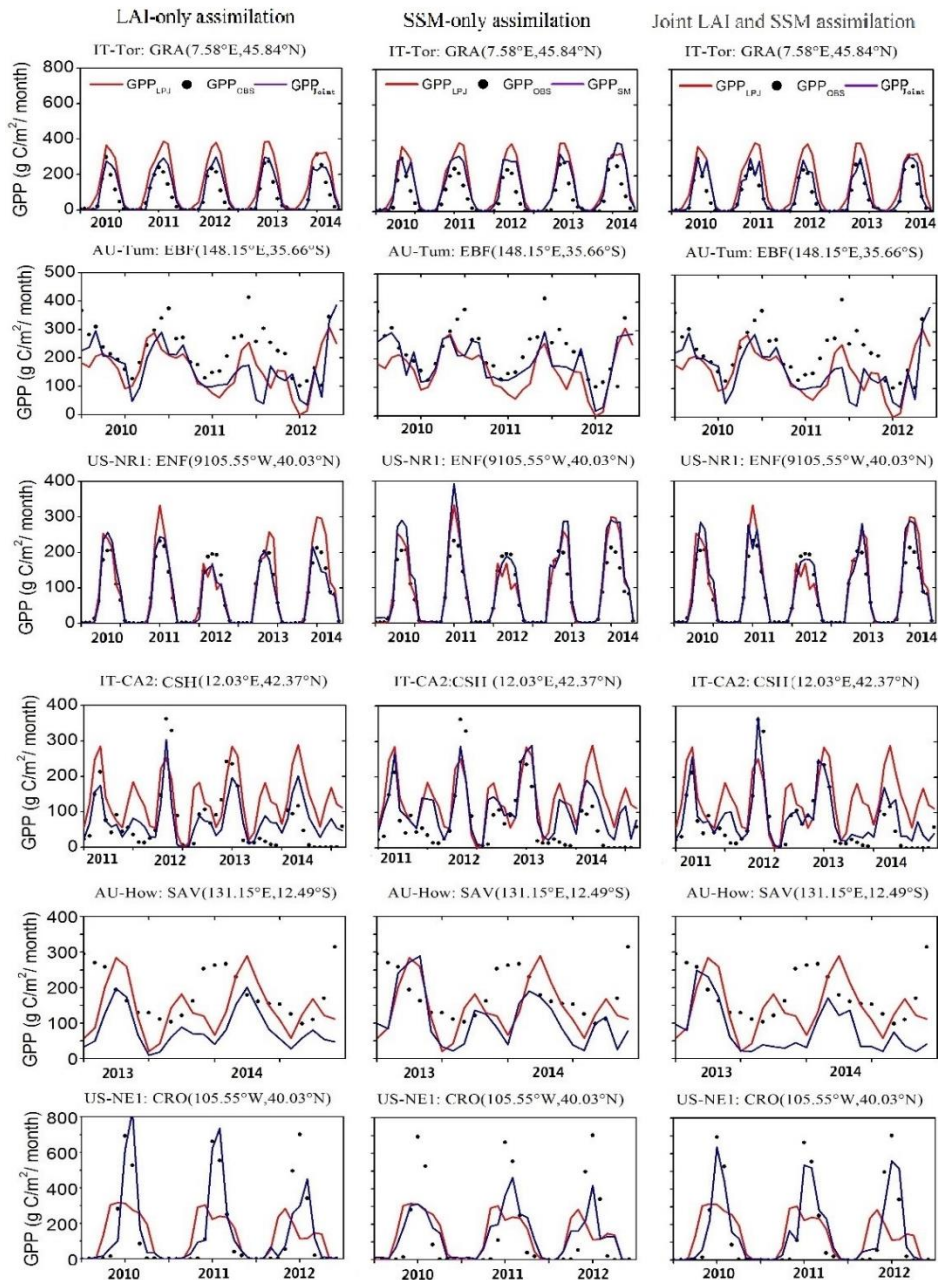
Figure 3. Seasonal cycles of tower GPP and simulated gross primary productivity (GPP) from Lund-Potsdam-Jena (LPJ), ~~GLASS LAI assimilation (scheme 1)~~LAI-only assimilation, ~~SMOS assimilation (scheme 2~~SSM-only assimilation~~)~~ and joint assimilation ~~(scheme 3)~~ for six sites representing six PFTs.

493   The residual analysis indicated that the three assimilation schemes for GPP (Figure ~~S11~~ S11 (left))

494 were different. For the assimilation results, most of the errors were distributed around $-70 \sim 60$ g C m^{-2}

495 month^{-1}. The high GPP$_{OBS}$ values were considerably underestimated. The maximum negative error

496 reached 100 g C m^{-2} month^{-1}. The error distribution of GPP$_{SM}$ was more dispersed than that of GPP$_{LAI}$

497 and ~~GPP$_{co}$~~ GPP$_{joint}$. Among the residuals of these three schemes, GPP$_{SM}$ significantly overestimated the

498 GPP$_{OBS}$, mainly distributed in the 0–200 g C m^{-2} month^{-1} range. GPP$_{LAI}$ showed significant improvement

499 in the overestimation of GPP$_{OBS}$ compared with ~~GPP$_{co}$~~ GPP$_{joint}$. In general, the GPP$_{joint}$~~GPP$_{co}$~~ with the

500 most concentrated error distribution had significant improvement.
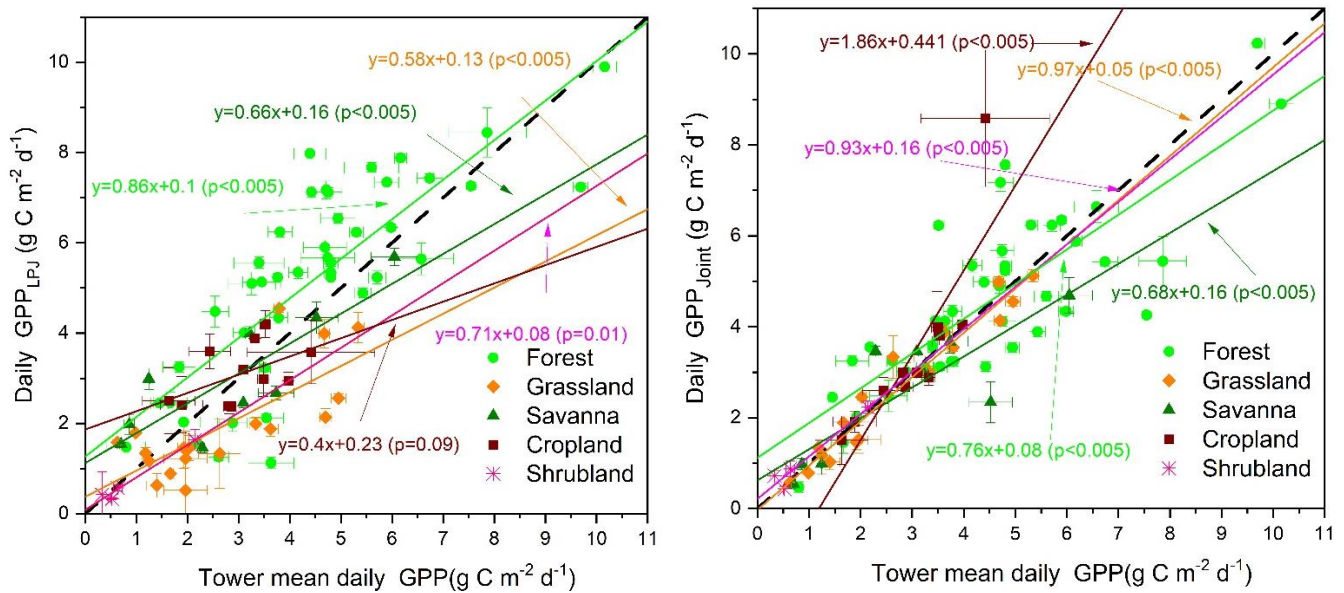
Figure 4. Scatterplots of daily GPP$_{LPJ}$ (left) and GPP$_{joint}$~~GPP$_{co}$~~ (right) versus tower GPP for different

PFTs.

504   After determining the optimal assimilation scheme (~~scheme 3~~Joint LAI and SSM assimilation

505   scheme), we evaluated the GPP_{LPJ} and GPP_{joint}~~GPP_{co}~~ at the site level (Figure.4). The results showed that

506   GPP_{joint}~~GPP_{co}~~ performed better (R^2= 0.83, ubRMSD= 1.15 g C m^{-2} d^{-1}) than GPP_{LPJ} (R^2= 0.69,

507   ubRMSD= 1.91 g C m^{-2} d^{-1}). The noticeable underestimation in all PFTs and overestimation at most forest

508   sites for GPP_{LPJ} were corrected by joint assimilation (GPP_{joint}~~GPP_{co}~~). Our joint assimilation methods

509   had better performance in forests, shrublands, and grasslands than in croplands and savannas. Except for

510   the cropland, the linear fitting results of other types were all below the 1:1 line, showing the overall

511   underestimation. Superior performance in both original simulation and assimilation occurred at shrubland

512   (R^2= 0.93, ubRMSD= 0.89 g C m^{-2} d^{-1}) and grassland (R^2= 0.97, ubRMSD= 0.83 g C m^{-2} d^{-1}) sites.

513   However, the standard deviation of GPP_{joint}~~GPP_{co}~~ and GPP_{OBS} at savanna sites was relatively large, and

514   the ~~assimilated GPP~~GPP_{joint}~~GPP_{joint}~~ at several savanna sites was significantly underestimated.

515   4.1.2 Accuracy assessment of ET for separate and joint assimilation

516   In general, the coefficient of determination (R^2) between ET_{LPJ} and ET_{OBS} was generally over 0.4

517   (the simulations were superior to GPP_{LPJ}) (Figure ~~5~~S6). ET_{LAI} showed slightly higher R^2, while some

518   sites showed reduced values (41 sites). The ET_{SM} and ~~ET_{co}~~ET_{joint} were significantly improved

519   compared with the ET_{LAI}. The R^2 increased considerably in Australia but declined at some sites in the

520   United States after assimilation. For ubRMSD, ET_{joint}~~$ET_{joint}ET_{co}$~~ performed better than ET_{SM} and

521 ET$_{LAI}$. The SSM assimilation improved more in humid regions, while the ubRMSD of ET$_{SM}$ was

522 slightly higher in South America (Figure 5). In the original LPJ-DGVM simulation, the sites with a

523 negative BIAS~~bias~~ were mostly located in the humid and ~~dry-sub~~sub-dry humid regions, while most of

524 the sites in arid and semi-arid regions had underestimation (Figure. ~~5~~S7- ~~BIAS~~(a), Table S3). The

525 assimilation improved ET at some of the overestimated sites, but the underestimation over these sites

526 showed little improvement.
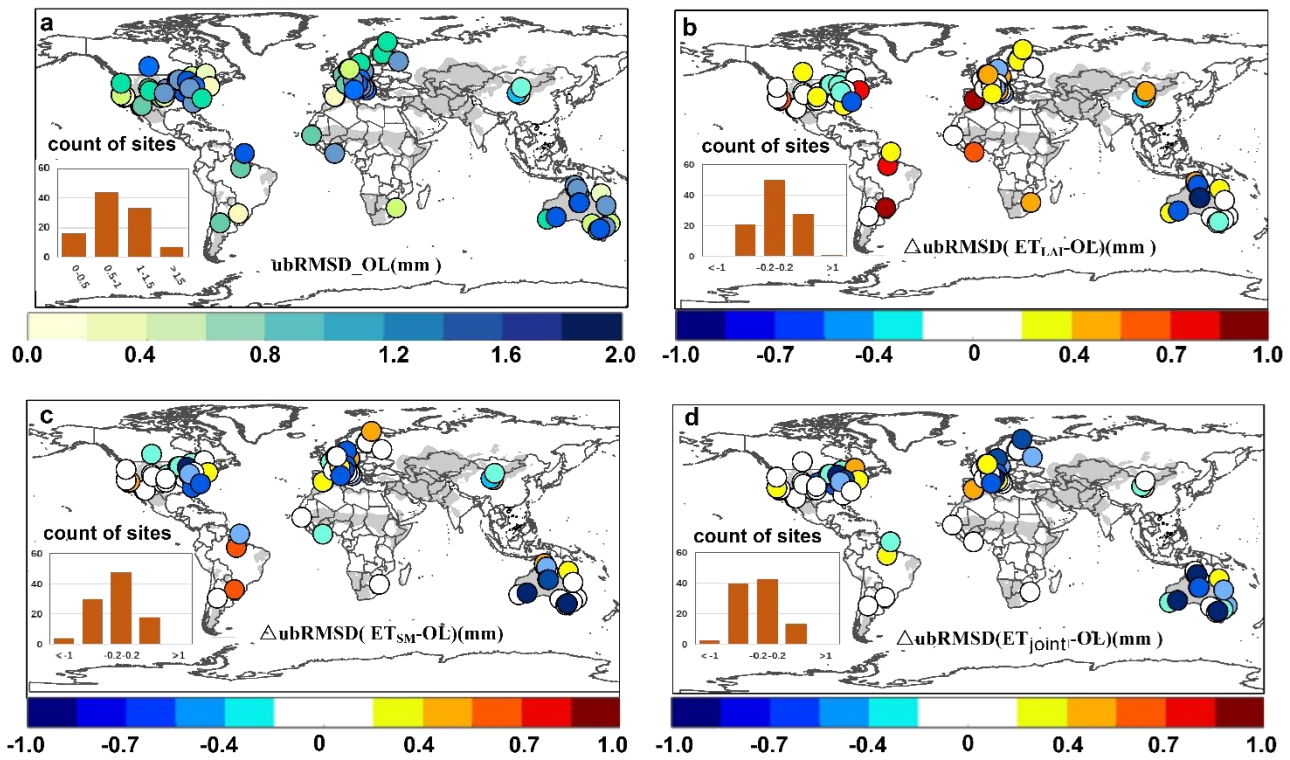
527

Figure 5 (a) The Unbiased Root Mean Square Error (ubRMSE) between the ET simulated by the LPJ-DGVM and the site observations, with yellow/blue indicating low/high ~~D~~ubRMSD; (b)△ubRMSD(ET$_{LAI}$-ET$_{LPJ}$);(c) △ubRMSD(ET$_{SM}$- ET$_{LPJ}$); (d)△ubRMSD(ET$_{Joint}$- ET$_{LPJ}$), blue/red represent positive/negative value.

528

529   At the seasonal scale, the model simulations were able to capture the temporal trend of ET_{OBS}, and

530   joint assimilation significantly improved the simulation in the growing season (US-NR1, US-NE1);

531   overall underestimation was observed for ET_{OBS}, especially in winter (Figure 6). Overall, the linear fitting

532   of monthly ET_{joint}~~ET_{co}~~ and ET_{OBS} was closer to 1:1 than that of ET_{LAI} and ET_{SM} (Figure S10). The

533   simulation accuracy of joint assimilation was better than that of separate assimilation, and the

534   performance of the SSM assimilation was better than that of the LAI assimilation.

535   The ET residual analysis (Figure ~~S7~~ S11 (right)) indicated that the three assimilation scheme errors

536   showed underestimation for ET_{OBS}. In general, the error distribution of separate assimilations was more

537   dispersed than that of the joint assimilation. Similar to the assimilation performance of GPP, ET_{joint}~~ET_{co}~~

538   and ET_{SM} significantly improved the overestimation of ET_{OBS}, but did not significantly improve the

539   underestimation. For the ET_{joint}~~ET_{co}~~, most of the errors were distributed around -30–18 mm month^{-1}.

540   The region with high ET_{OBS} was considerably underestimated, and the maximum negative error reached

541   −57 mm month^{-1}.

542   We also evaluated the ET assimilation results at the PFT scale (Figure 7). The results showed that

543   our ET values resulting from the assimilation~~assimilated ET~~ performed better at the site level (R^2= 0.77,

544   ubRMSD= 0.65 mm d^{-1}) than that of ET_{LPJ} (R^2= 0.67, ubRMSD=0.95 mm d^{-1}). Joint assimilation

545   significantly reduced the errors of those shrubland sites with overestimation for ET_{OBS}, and the site

546   distribution was closer to the 1:1 line. Our assimilation methods had better performance in forest, savanna,

547   and grassland ecosystems than in cropland and shrubland (Table S3). The linear fitting results of grassland

548   and shrubland were all above the 1:1 line, showing overall overestimation. Although the original

549   simulation and assimilation performance were superior at savanna sites (R^2= 0.95, ubRMSD= 0.78 mm

550   d^{-1}), the standard deviations of ET_{joint} ~~ET_{co}~~ and ET_{OBS} at savanna sites were relatively large, which was

551   similar to the GPP results at savanna sites.

552
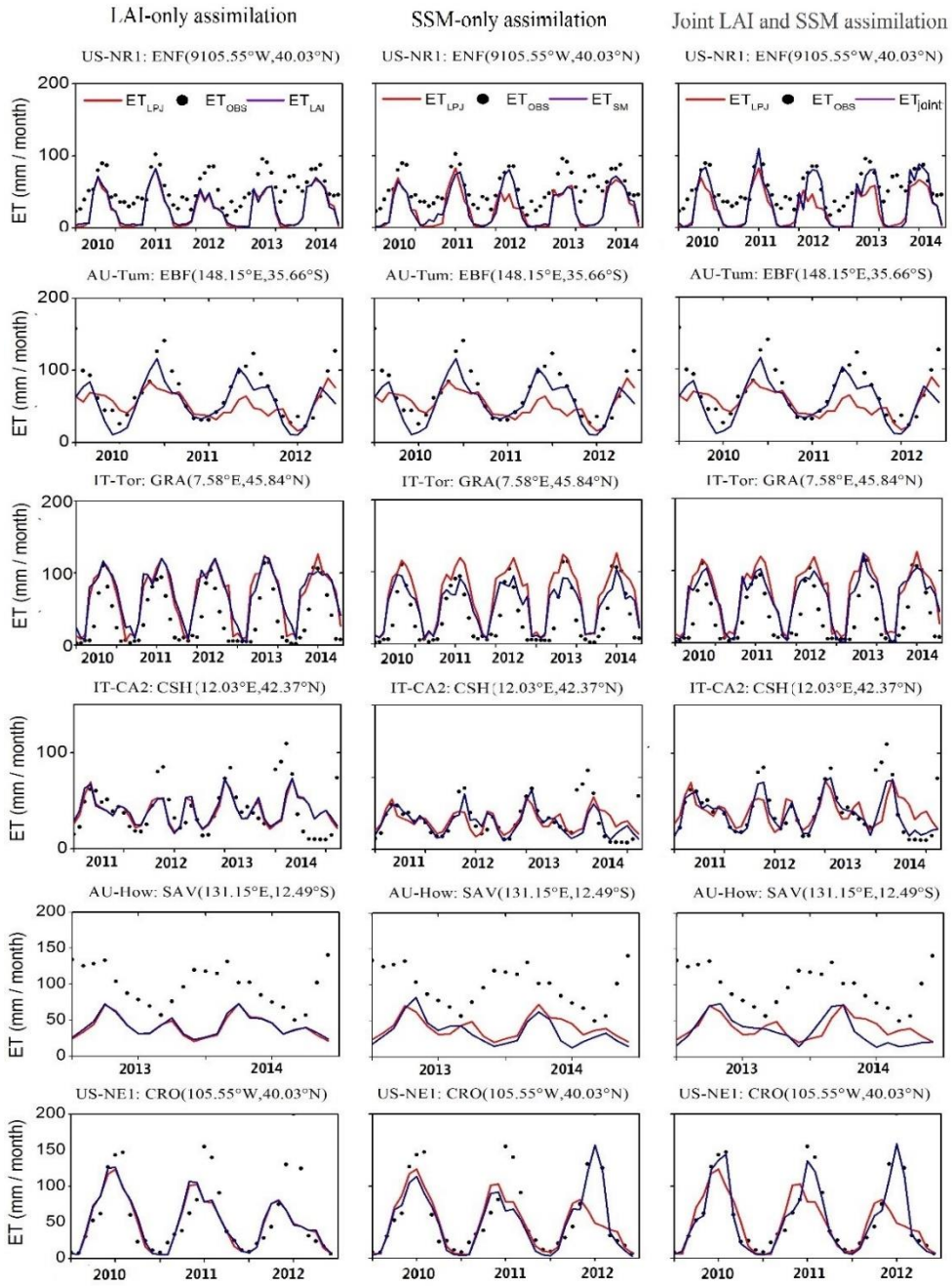
Figure 6. Seasonal cycles of tower-based and simulated ET from Lund-Potsdam-Jena (LPJ), ~~GLASS LAI~~

554 ~~assimilation (scheme 1~~**LAI-only assimilation**~~)~~**,** **SSM-only assimilation** ~~SMOS assimilation (scheme 2)~~ **and**

555 **joint assimilation** ~~(scheme 3)~~ **for the six sites representing six PFTs during the study period.**
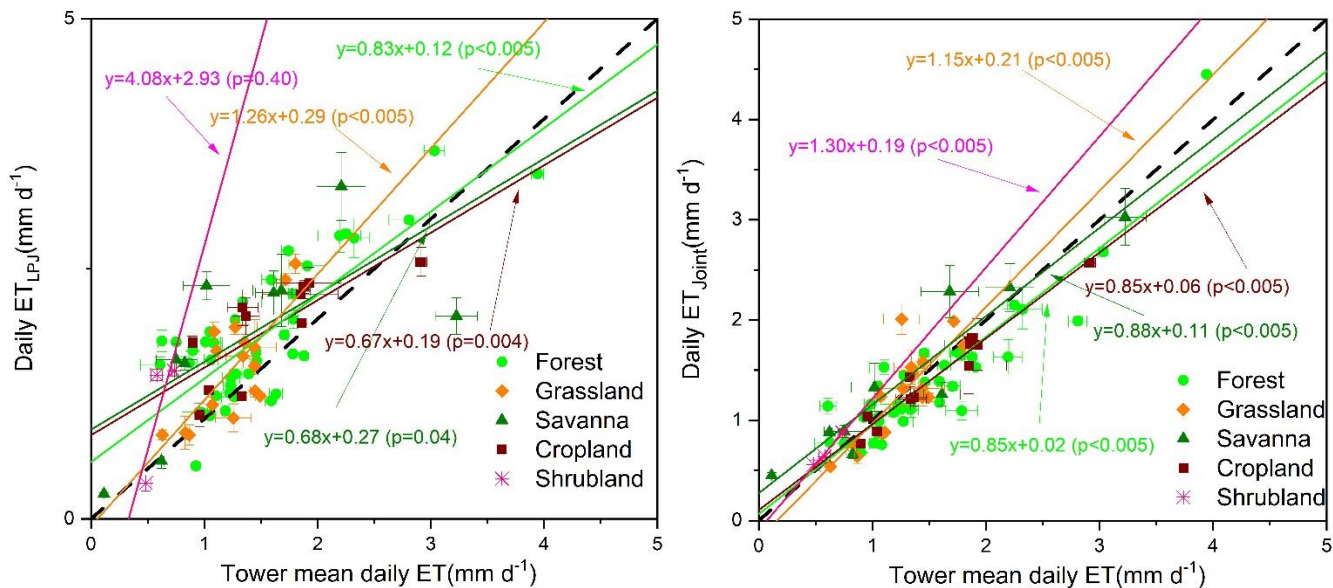
557 **Figure 7. Scatter plots of daily ETjoint~~ETₑₒ~~ versus tower ET under different PFTs.**

558 *4.2. Comparison of assimilation performance in semi-arid and arid regions with that in humid and* ~~dry~~

559 ~~sub~~*sub-dry humid regions*

560
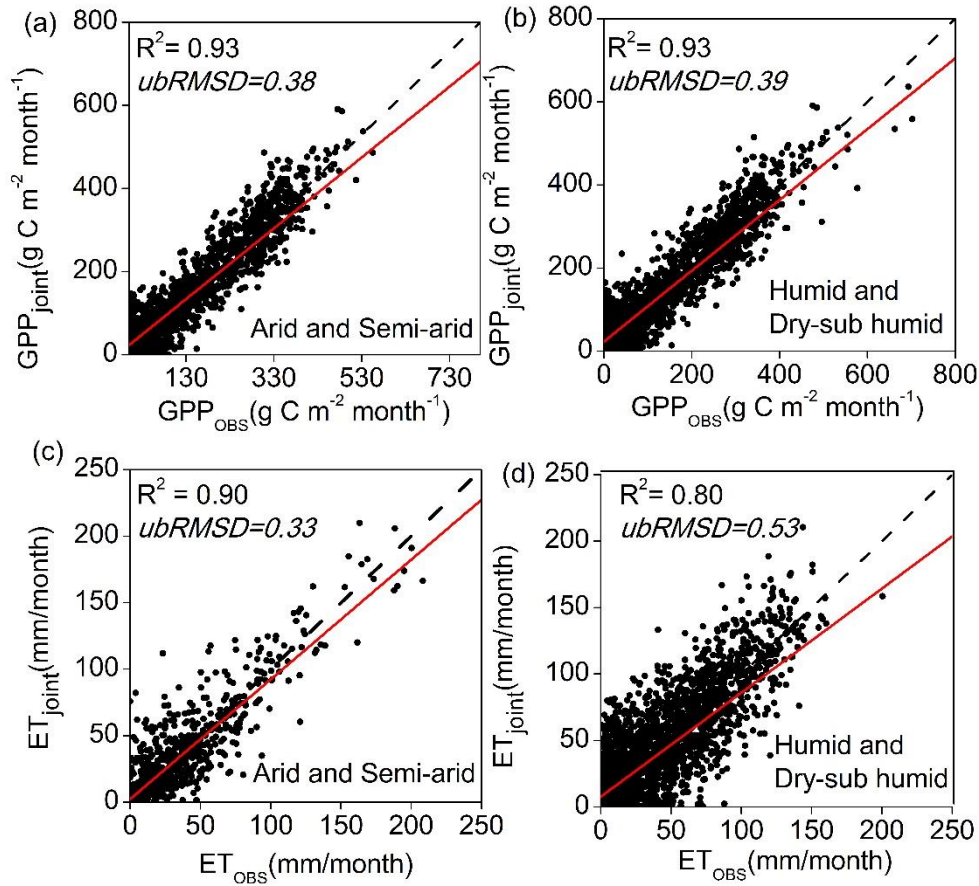
Figure 8. Scatter plots of daily tower GPP and ET versus ~~GPPco~~GPPjoint and ~~ETco~~ETjoint under arid and humid sites: (a) and (c) are the fitting results of GPP and ET in arid and semi-arid regions, respectively; (b) and (d) are the fitting results of GPP and ET in humid and dry sub-humid zone, respectively.

During the period 2010–2014, monthly ~~GPPco~~GPPjoint and ~~ETco~~ETjoint performed differently in humid and sub-dry humid regions and semi-arid and arid regions (Figure 8, Table S2,3). Overall, the GPP and ET simulations had good consistency with the tower data in the two regions. For

567 GPP$_{joint}$~~GPP$_{joint}$~~~~GPP$_{co}$~~, there was no significant difference in the correlation and fitting coefficients

568 between the two regions. As for ET$_{joint}$~~ET$_{co}$~~, the fitting results and R^2 values in the semi-arid and arid

569 regions performed better than those in the humid and sub-dry humid regions, which also suggested the

570 importance of ~~surface~~ SSM for ET estimation in water-limited areas.

571   On the daily scale, the original GPP simulations (GPP$_{LPJ}$) performed better in the semi-arid and

572 arid regions than in the humid and sub-dry humid regions with higher R^2 and lower ubRMSD (Table S2).

573 the R^2 and BIAS~~bias~~ implied that the LAI assimilation alone had a better performance than the SSM

574 assimilation alone. However, for sites in arid and semi-arid areas, the ~~RMSD and~~ ubRMSD showed that

575 the GPP$_{SM}$ improved better than GPP$_{LAI}$, which both demonstrated SSM data are essential in water-limited

576 regions. For GPP$_{joint}$~~GPP$_{co}$~~, the shrubland in the semi-arid and arid regions had the lowest R^2 values and

577 the second lowest ubRMSD. The forest in the semi-arid and arid regions had the largest improvement

578 after assimilation. In the humid and sub-dry humid regions, the GPP$_{joint}$~~GPP$_{co}$~~ of the savanna and

579 cropland showed the largest improvement (R^2 increased by 64.7% and 71.1%, respectively; ubRMSD

580 decreased by 47.0% and 31.8%, respectively). The grassland in the semi-arid and arid regions had the

581 highest R^2, and the savanna by combining all indicators had the best assimilation results compared to

582 other types in both regions.

583   Similar to ET$_{joint}$~~ET$_{co}$~~, the ET$_{LPJ}$ in the semi-arid and arid regions was better than that in humid and

584 sub-dry humid regions in terms of four evaluation indicators (ubRMSD decreased by 34.4% in semi-arid

585 and arid regions and the ubRMSD decreased by 30.9% in humid and sub-dry humid regions compared

586 with ET$_{LPJ}$). The R^2 and ubRMSD implied that the SSM assimilation alone had a better performance than

587 the LAI assimilation alone, especially for sites in arid areas. and the BIASbias showed that the ET$_{LAI}$

588 improved better than ET$_{SM}$ for sites in humid and sub-dry humid areas. The performance of the original

589 simulation and assimilation of grassland sites in the semi-arid and arid regions was the best among all

590 five PFTs.

591

592
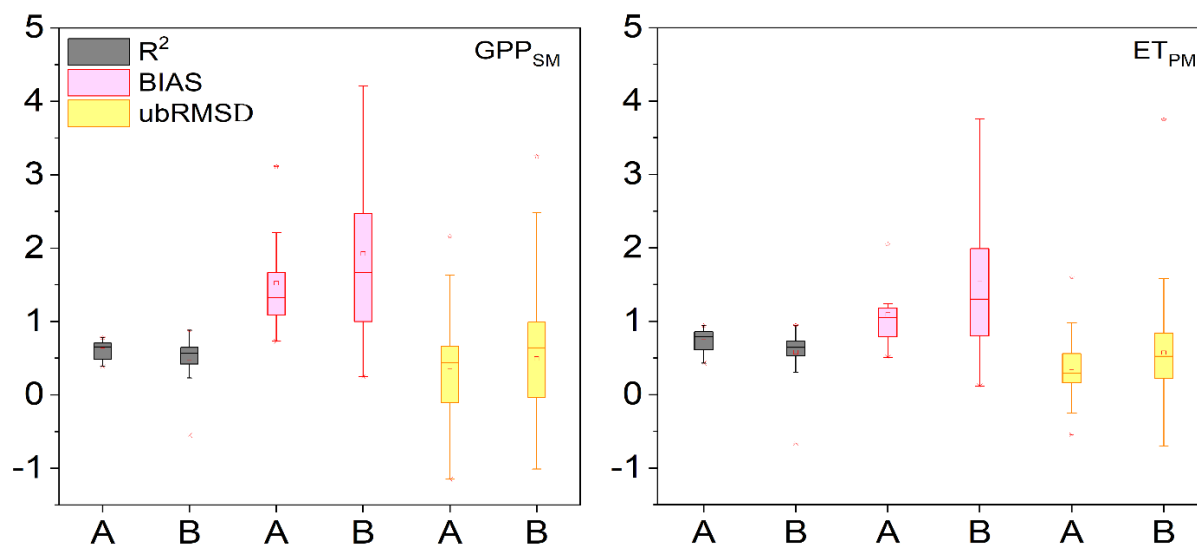
Figure 9. Boxplots of R^2, ubRMSD and BIAS for GPP$_{SM}$ (left) and ET$_{PM}$ (right). A represents the sites in arid

and semi-arid areas, and B represents the sites in humid and dry sub-humid areas.

595   To investigate the reasons for better assimilation performance in water-limited regions, we evaluated

596 the GPP and ET simulated by the LPJ-PM according to R^2, ubRMSD, and BIAS (Figure 79). Compared

597 with the semi-arid and arid regions, the humid and sub-dry humid region had smaller R^2 mean, larger

598   BIAS, and no significant difference in mean ubRMSD for GPP$_{SM}$. In general, the evaluation results of

599   joint assimilation for ET$_{PM}$ were generally consistent with those for GPP$_{SM}$ and GPP$_{SM}$. ET$_{PM}$ showed

600   underestimation, which was consistent with the underestimation in SSM assimilation. These results

601   indicated that, both GPP and ET modeled by LPJ-PM with joint assimilation were less stable and had a

602   lower performance in the humid and sub-dry regions than in the semi-arid and arid regions.

603   *4.3. Comparison of assimilation performance in assimilating SMOS and SMAP soil moisture data*
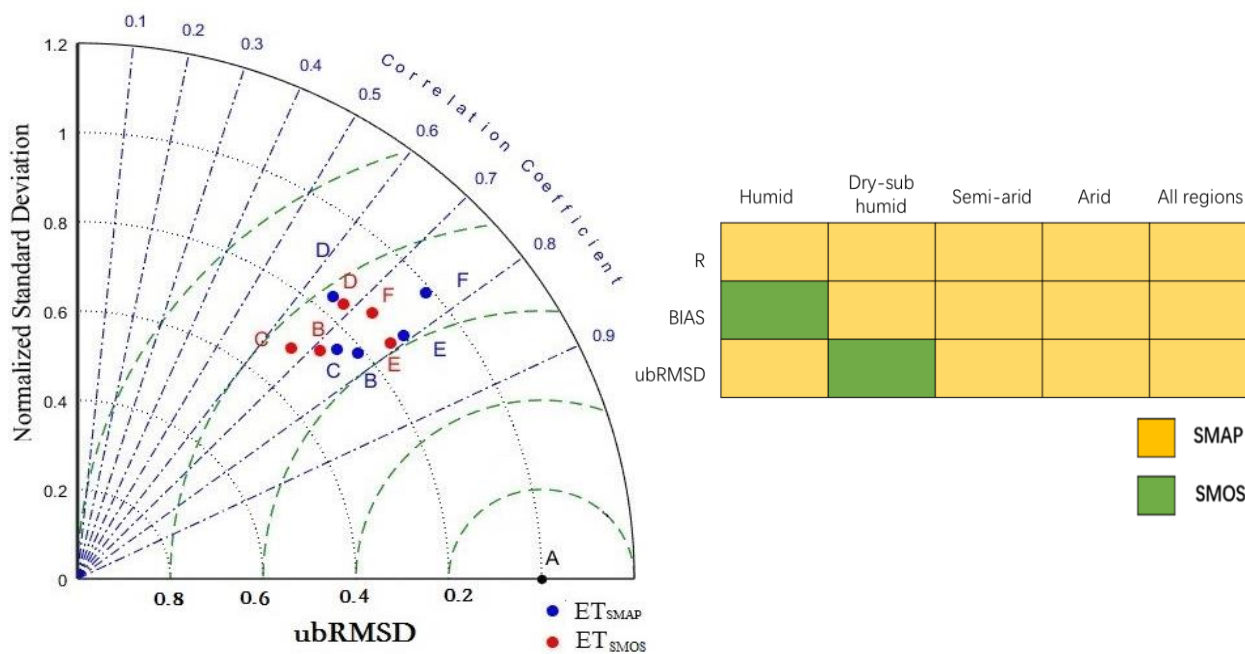
604

605   **Figure 10. Taylor diagram (left) comparing ET simulations with observations at all 46 AmeriFlux sites**

606   **at the daily time step between April 2015 and December 2018. Blue dots represent results based on**

607   **assimilation with SMAP SSM only and red dots represent results based on assimilation with SMOS SSM**

608   **only. ubRMSD refers to the dashed green lines. Reference points A and B-F correspond to the vegetation**

functional types (PFTs). The grid diagram (right) compares the evaluation indices of ET simulations with those of the observed values at all 46 AmeriFlux sites with different wet and dry zones at the daily time step; the yellow cells indicate that ET$_{SMAP}$ performs better in the metric, and green cells indicate that ET$_{SMOS}$ performs better in the metric.

The Taylor chart was used to compare the assimilation performance of ET$_{SMAP}$ and ET$_{SMOS}$ at 46 AmeriFux sites (Figure 10-left). The results showed that ET$_{SMAP}$ performed better than ET$_{SMOS}$ for ~~all~~ most PFTs, except forest. Both ET$_{SMAP}$ and ET$_{SMOS}$ performed well for grassland (closer to point A), and there was little difference between R^2 and ~~standardized~~ ubRMSD. The NSD of ET$_{SMAP}$ in grassland was 0.88, which was closer to 1 than that of ET$_{SMOS}$. The assimilation of ET in the forest had a lower R^2 and higher ~~standardized~~ ubRMSD (0.7-0.8) than those of other PFTs, and the NSD of cropland and shrubland was lower than that of other PFTs (0.6-0.8), indicating that the assimilation for cropland and shrubland could not reproduce the variations in ET effectively. However, ET$_{SMAP}$ showed significant improvement in R^2 compared with ET$_{SMOS}$ for shrubland and cropland. The assimilation performance of ET$_{SMAP}$ and ET$_{SMOS}$ for savanna showed the greatest difference. In general, the ET$_{SMAP}$ and ET$_{SMOS}$ were slightly different, and the ET$_{SMAP}$ was more improved than ET$_{SMOS}$.

Figure 10 (right) shows the assimilation accuracy of ET$_{SMOS}$ and ET$_{SMAP}$ in different humid and arid regions. The ET$_{SMAP}$ had significant advantages for the four indicators. The R^2 of ET$_{SMAP}$ was higher than that of ET$_{SMOS}$ in all the areas. However, ET$_{SMOS}$ in some evaluation indicators showed a better performance than ET$_{SMAP}$ (BIAS in the humid region; ubRMSD in the sub-dry humid region). This may be due to the overall more humid nature of SMOS SSM than the SMAP SSM. Moreover, the sensitivity of deep soil moisture contributed more to the ET in humid areas than in the water-limited areas.

630 *4.4. Global simulations of GPP and ET with joint assimilation of LAI and soil moisture data*

631   To assess the spatial scalability of the LPJ-VSJA assimilation scheme, we simulated the global daily

632 GPP and ET for 2010–2018 with a spatial resolution of 0.25°. The original results simulated by the LPJ-

633 DGVM and LPJ-VSJA were referred to as LPJ-DGVM GPP(ET) and LPJ-VSJA GPP(ET), respectively.

634 We compared the annual spatial GPP and ET values and the error standard deviation of the LPJ-VSJA

635 with several existing flux products.

636   Figures 11 and 12 depict the spatial distribution of the annual mean and the differences between our

637 simulation results and the global independent satellite-based products. The developed LPJ-VSJA GPP

638 was the closest to GOSIF GPP (Li and Xiao 2019) in most regions with the lowest spatial mean deviation

639 (LPJ-VSJA-GOSIF) (27.9 g C m^{-2} yr^{-1}), followed by GLASS GPP (51.2 g C m^{-2} yr^{-1}) (Yuan et al. 2010),

640 LPJ-DGVM (-73.4 g C m^{-2} yr^{-1}), and MODIS GPP (93.1 g C m^{-2} yr^{-1}). LPJ-VSJA had higher GPP values

641 than GOSIF GPP in tropical regions, such as Amazonia, Central Africa, and Southeast Asia. In general,

642 the annual mean and differences between MODIS, GOSIF GPP, LPJ-DGVM, and our LPJ-VSJA were

643 in broad agreement (with higher R^2 ranging from 0.74 to 0.95).

644   LPJ-VSJA ET was the closest to GLEAM ET on the spatial average with the least spatial average

645 deviation (-13.9 mm yr^{-1}) and highest R^2 (0.88), followed by GLASS ET (-23.1 mm yr^{-1} and 0.82), GLDAS

646 ET (-34.7 mm yr^{-1} and 0.73), LPJ-DGVM (-48.7 and 0.66 mm yr^{-1}), and MODIS ET (-122.1and 0.54 mm

647 yr^{-1}).
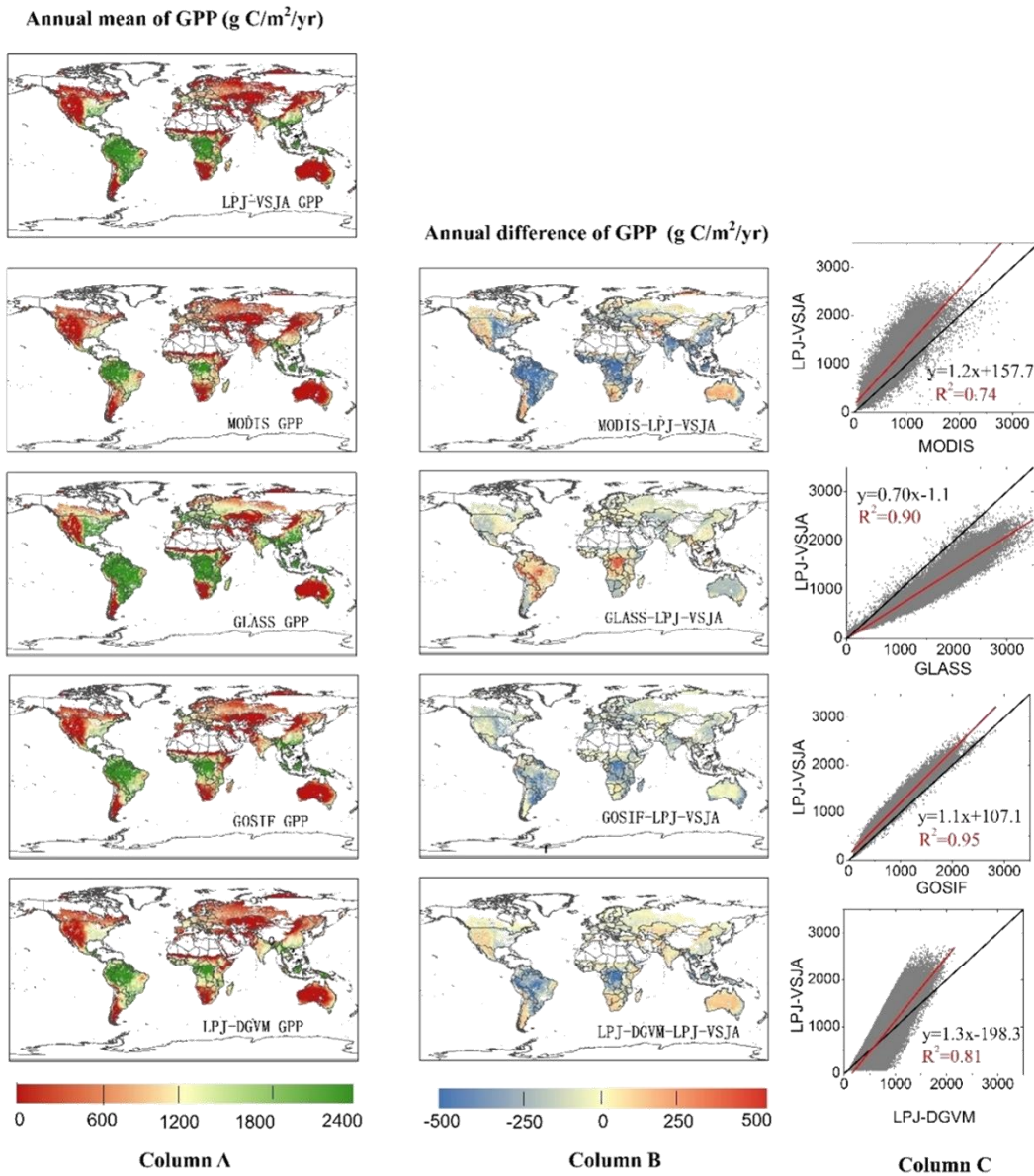
Figure 11. Column A: Spatial distribution of annual LPJ-VSJA GPP and other independent satellite-based datasets (a: MODIS GPP; b: GLASS GPP; c: GOSIF GPP; e: LPJ-DGVM). Column B: Spatial distribution of the difference between annual LPJ-VSJA GPP and other independent satellite-based

652   **datasets. Column C: Scatter plots between these products. Black lines show the 1:1-line, red lines show the**

653   **regression fit.**

654
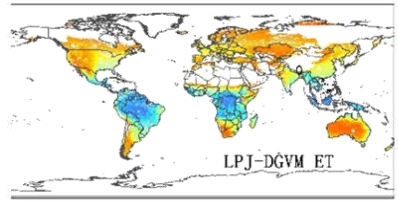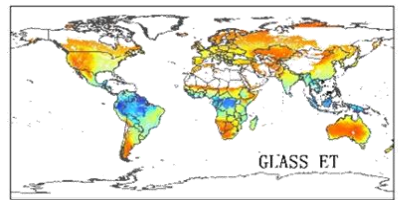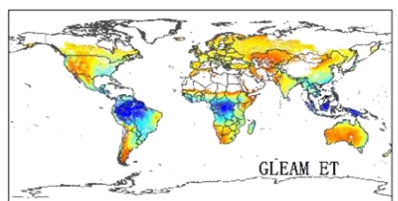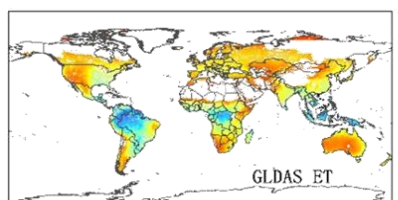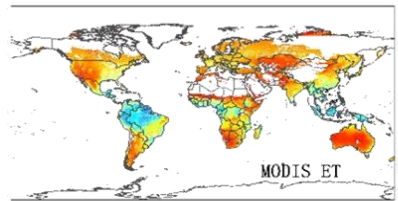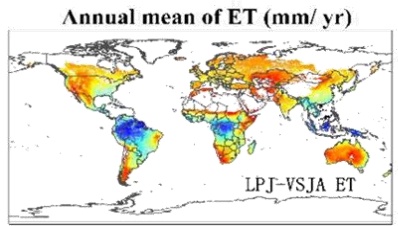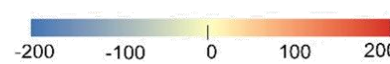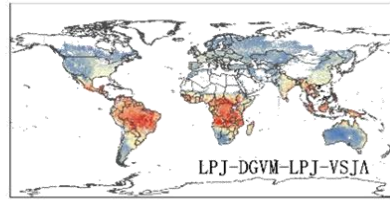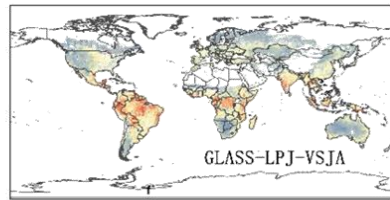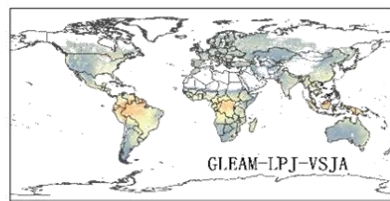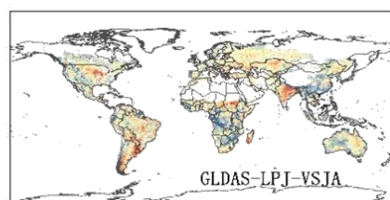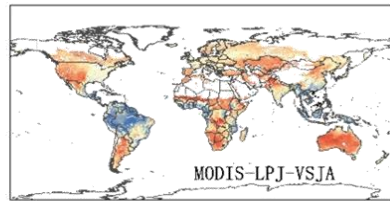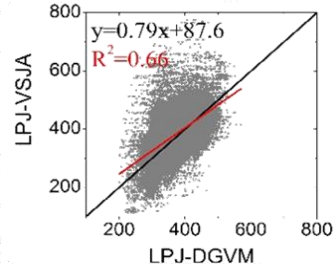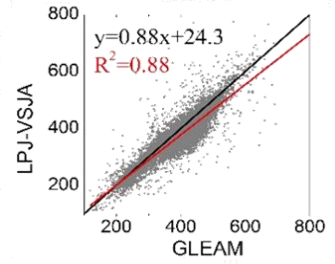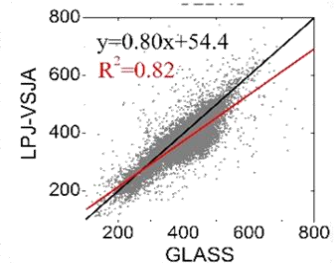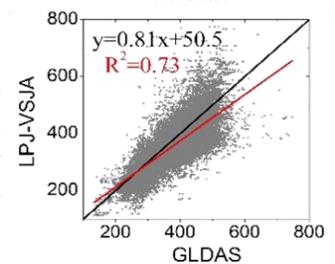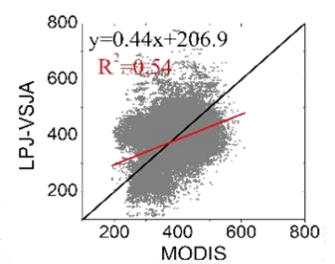
655   **Figure 12. Column A: Spatial distribution of annual LPJ-VSJA ET and other independent satellite-**

656   **based datasets (a: MODIS GPP; b: GLDAS ET; c: GLEAM ET; d: GLASS ET; e: LPJ-DGVM ET).**

657   **Column B: Spatial distribution of the difference between annual LPJ-VSJA ET and other independent**

658   **satellite-based datasets. Column C: Scatter plots between these products are provided on the right of the**

659   **difference maps. Black lines show the 1:1-line, red lines show the regression fit.**

660

661   Figure 13 (a)–(e) represent the spatial error standard deviation (σ) distribution of MODIS, GLASS,

662   GOSIF, and LPJ-VSJA GPP, respectively. The graphs on the right side depict the corresponding

663   histograms. The σ of the MODIS GPP was evenly distributed between 30 and 60 g C m^{-2} month^{-1}, while

664   the average σ of other products was concentrated in 0–20 g C m^{-2} month^{-1} (90%). The high errors of all

665   products were concentrated in the high temperature and humid areas of southern North America, eastern

666   South America, humid and dry sub-humid areas of South Asia, and the savannas of Africa and Australia.

667   The error histogram of GOSIF GPP and LPJ-DGVM GPP were in line with the normal distribution, with

668   an average value of 8.3 g C m^{-2} month^{-1} and 22.4 g C m^{-2} month^{-1}. The GLASS GPP product had the

669   lowest mean value (3.6 g C m^{-2} month^{-1}), followed by LPJ-VSJA (4.7 g C m^{-2} month^{-1}), but the error

670   variance of the LPJ-VSJA product was the lowest, indicating a stability of the regional error (Table S4).

671   Compared to the LPJ-DGVM, the joint assimilation results showed improvement in all regions (the

672   average error reduced by 17.7 g C m^{-2} month^{-1}), especially in the humid regions of South Asia, Australia,

673   and the United States. Our LPJ-VSJA GPP was generally proven to have high accuracy and stability for

674   spatial analysis and could provide a reference for other model products.
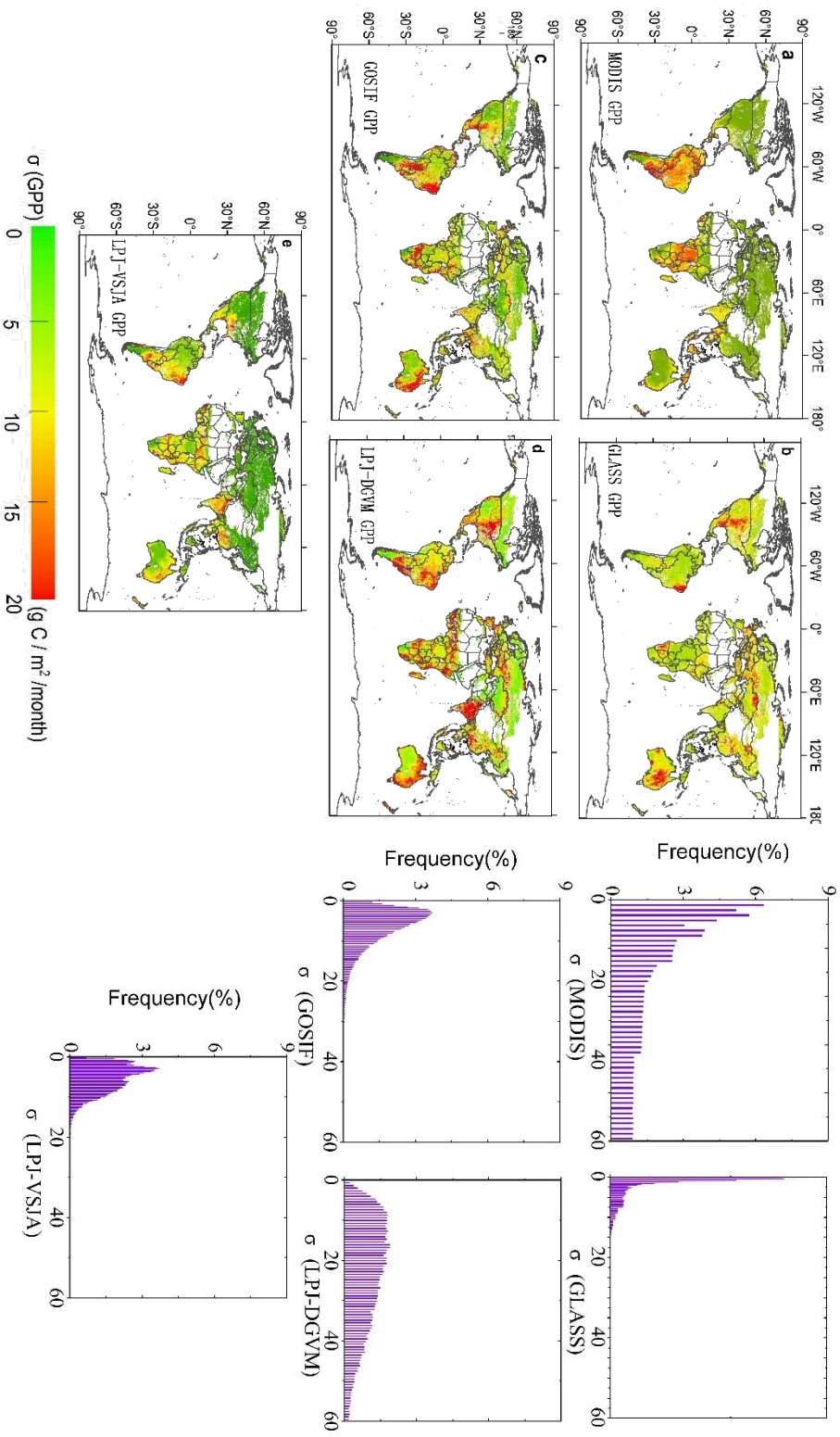
Figure 13. Spatial distribution and histograms of error standard deviation (σ) for global GPP products: MODIS (a), GOSIF (b), GLASS (c), LPJ-DGVM (d), and LPJ-VSJA (e).

675
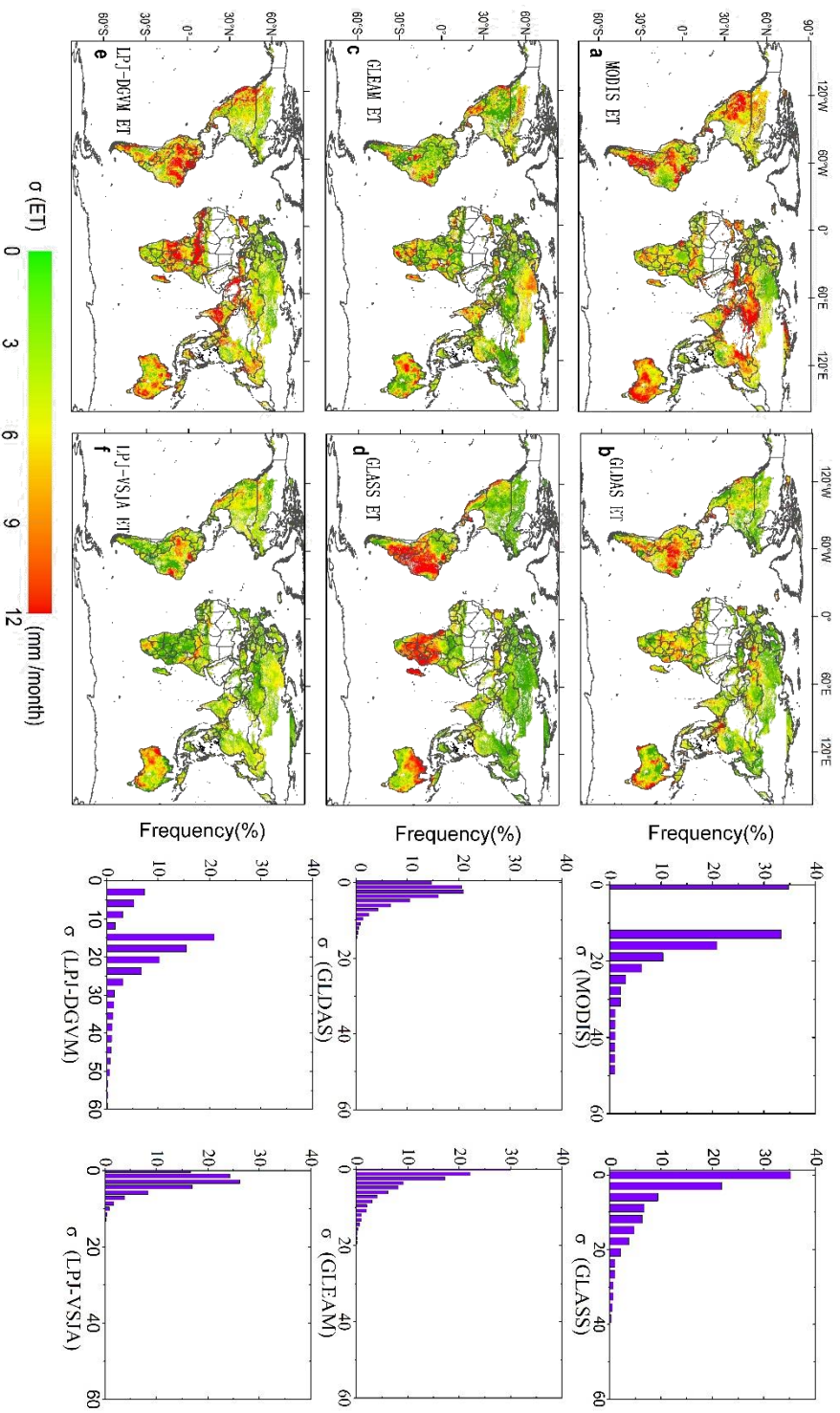
Figure14. Spatial distribution and histograms of error standard deviation (σ) for global ET products: MODIS (a),GLDAS (b),GLEAM (c), GLASS (d), LPJ-DGVM (e), and LPJ-VSJA (f).

676

677   Figures 14 (a)–(f) show the σ of MODIS, GLDAS, GLEAM, GLASS, and LPJ-VSJA ET (the units

678   are mm/month), and the right graphs are the corresponding histograms. The σ values of GLDAS and LPJ-

679   VSJA represented a normal distribution trend. Except for MODIS, GLASS, and LPJ-DGVM (0–60 mm

680   month^{-1}), the σ of other products was generally between 0-20 mm month^{-1}. The simulation error was

681   relatively smaller in the Northern Hemisphere than in the Southern Hemisphere, especially for GLASS

682   ET and GLDAS ET. Significant improvements in joint assimilation were observed in the northern

683   hemisphere (especially in the semi-arid areas of the western United States and savanna and cropland areas

684   of central India) and African savanna areas, and the average error was reduced by 15.1 mm month^{-1}. In

685   general, the error mean and variance of LPJ-VSJA and GLEAM products were relatively low (Table S4),

686   and there was no apparent extremely high value region in the error distribution. Among the five products,

687   LPJ-VSJA had the lowest error mean and variance and the highest accuracy.

5. Discussion

5.1 Advantage of joint assimilation for GPP and ET

The benefit of employing multiple data flows in an assimilation system is the complementarity of the data, which enables constraints on different components of the underlying process-based terrestrial biosphere model. Due to the interaction and feedback between the internal components of the model, the assimilation of multiple observations has a synergistic effect, and the integrated constraints are greater than the individual constraint (Kato et al. (2013)). The advantage of our joint assimilation is that it can improve the simulation accuracy of both GPP and ET, especially ET, in arid and semi-arid regions.

In the GPP assimilation experiment, the performance of the LAI assimilation was better than that of the SSM assimilation possibly for two reasons: (1) the LPJ-VSJA is more controlled by LAI data because the ratio of assimilated LAI (daily input) to SSM observations (3-day interval input) is approximately 3:1, which makes the likelihood function biased to LAI data; (2) the SM directly influences the simulation of ET, and the corresponding time function (computes the top layer SM (50 cm)) used here by Zhao et al. (2013)will result in the error of the updated top SM and propagating the error to the GPP$_{SM}$. In addition, the 8-day interval LAI has the capability to capture the temporal variability of phenology.

Current studies on terrestrial water and carbon flux assimilation mostly focus on the assimilation between a single model framework and observation results, lacking the fusion and comparison between multiple models. The processed models used in DA are simplifications and approximations of reality, and different models focus on different ecological processes. In this study, the updated ET module was

707 integrated to compensate for the simplification of soil stratification and the lack of SM information in the

708 hydrological module of the LPJ-DGVM. Therefore, the integration of multiple types of models and multi-

709 source observation data (remotely sensed data, ecological inventory data (National Ecological

710 Observatory Network, NEON (Keller et al. 2008)), and other measurements (Desai et al. 2011; Hayes et

711 al. 2012) is expected to more objectively and effectively simulate the real state of ecosystems.

712 *5.2 Comparison of joint assimilation (LPJ-VSJA) and other models for GPP and ET across regions and*

713 *vegetation types*

714   Global GPP and ET for different products were calculated by multiplying the global mean GPP

715 density flux with the global vegetation area (122.4 million km^2) originated from the MODIS land cover

716 product (Friedl et al. 2010). The mean global GPP of the LPJ-VSJA (130.2 Pg C yr^{-1}) was

717 approximately 12% lower than that of PML-V2 (145.8 Pg C yr^{-1}) and 18% higher than that of GLASS

718 and MODIS, respectively (Table S6). The GPP values of LPJ-VSJA and GOSIF were the most similar.

719 The GOSIF GPP was developed from gridded SIF using simple linear relationships between SIF and

720 GPP. Our global LPJ-VSJA GPP estimates were within the currently most plausible 110–150 Pg C/yr

721 range.

722   As for ET, our results were similar to those of GLEAM ET and lower than those of PML-V2,

723 GLDAS-2, and GLASS ET (~72000 ~~mm~~ km^2 yr^{-1}). Joint assimilation improved the overestimation of

724 LPJ-DGVM ET. At the daily scale, the estimation accuracy of PML-V2 and GLDAS-2 products,

725 calibrated with flux tower data, was better than that of our estimates, which suggests an underestimation

of LPJ-VSJA ET in wet regions. It is likely because the SSM of SMAP or SMOS was underestimated in the wet region or the influence of deep SM was under-represented. According to Seneviratne et al. (2010), satellite-based ET estimation approaches often overestimate ET in areas of arid and semi-arid climatic regimes in the magnitude of 0.50 to 3.00 mm d^{-1}. The poor performance of these models can largely be attributed to the lack of constraints of SSM or RZSM and more accurate vegetation parameters (Gokmen et al. 2012; Pardo et al. 2014). For instance, the monthly estimated ET modeled by the Penman-Monteith-Leuning (PML) model agreed with flux tower data well (R^2 = 0.77; BIAS~~bias~~ = − 9.7%, approximately 0.2 mm d^{-1}). Our annual ET simulations were lower than other products and slightly underestimated tower ET with a BIAS~~bias~~ of 0.19 mm d^{-1} (ET$_{OBS}$- ET$_{joint}$~~ETjointET$_{co}$~~).

In general, GPP and ET had better assimilation performance in arid and semi-arid regions than in humid and sub-dry ~~semi~~ -humid regions likely because of the following reasons. First, the incorporation of ~~surface~~ SSM is more important for vegetation growth in water-limited areas. The module PT-JPL$_{SM}$ has been proven to have better performance in semi-arid and arid regions (Purdy et al. 2018). Our integrated model LPJ-PM also performed better in semi-arid and arid regions by assimilating SMAP soil moisture (Li et al. 2020). Second, the input performance, including SMOS and SMAP SSM products, is better in arid and temperate regions than in cold and humid regions (Zhang et al. 2019). Third, the vegetation types in humid regions are more complex and relatively less accurately simulated by the LPJ-DGVM within a single grid cell. For comparison, Zhang et al. (2020) used a data-driven upscaling approach to estimate GPP and ET in global semi-arid regions. This data-driven approach (R^2 = 0.79, RMSD = 1.13 g C m^{-2} d^{-1}) had slightly higher performance in estimating GPP than our LPJ-VSJA (R^2

746 =0.73 and RMSD= 1.14 g C m^{-2} d^{-1}) and   the data-driven method ($R^2 = 0.72$ and RMSD = 0.72mm d^{-1})

747 had identical performance for estimating ET with our LPJ-VSJA(R^2 =0.73 and RMSD= 0.72 mm d^{-1}).

748   Our assimilation performance varied with PFT. The GPP and ET assimilation results of savanna sites

749 performed well in both dry and wet regions, and those of shrubland sites showed the most remarkable

750 improvement for simulations of LPJ-DGVM. The original simulation and assimilation performance of

751 grassland sites in the semi-arid and arid regions were the best for all five PFTs. Consistent with our

752 research, previous studies also showed better GPP or ET simulations for grassland, savannas, and

753 shrublands biomes. For instance, Feng et al. (2015) validated five satellite-based ET algorithms for semi-

754 arid ecosystems and concluded that all the models produced acceptable and relatively better results for

755 most grassland, savanna, and shrubland sites. Yang et al. (2017) demonstrated that he GLEAM ET had a

756 superior performance for the grassland sites. The GOSIF GPP demonstrated better simulation for

757 grassland and woody savannas sites at 8-day time steps with higher R^2 (0.77 and 0.83, respectively) and

758 lower RMSD (1.48 g C m^{-2} d^{-1} and 1.1 g C m^{-2} d^{-1}) (Li and Xiao 2019). In contrast, our LPJ-VSJA GPP

759 showed an R^2 of 0.87 for grassland and 0.75 for savannas and an RMSD of 1.11 g C m^{-2} d^{-1} and 1.1 g C

760 m^{-2} d^{-1}, respectively, in semi-arid and arid regions.

761 *5.3 Uncertainty analysis of joint assimilation*

762   Our validation results at both site and regional scales indicated that uncertainty existed in LPJ-VSJA

763 daily GPP and ET estimates. The errors from the tower EC observations, model-driven data, model

764 structure, error of satellite-based observations (e.g., LAI and SSM), and the spatial scale mismatch

765 between the ground observed footprint size and satellite-derived footprint size were the vital factors

766 affecting assimilation performance.

767   First, recent studies have revealed errors in the GLASS LAI and SMOS or SMAP SSM compared

768 with ground measurements. By computing the RMSD and R^2 of each product, the GLASS LAI accuracy

769 was clearly superior to that of MODIS and Four-Scale Geometric Optical Model based LAI (FSGOM) in

770 forests and GLASS and FSGOM led to in much higher annual GPP and ET estimates compared to

771 MCD15(Liu et al. 2018). The vegetation type (or land cover) misclassification caused 15–50% differences

772 in LAI retrieval (Fang and Liang 2005; Gonsamo and Chen 2011). Yan et al. (2016) calculated a RMSD

773 of 0.18 for the GLASS LAI over a range of HeiHe river~~drainage~~ basin sites and used the error to improve

774 the simulation of LAI and fluxes by assimilating GLASS LAI data. Previous studies reported an

775 improvement in the performance of the SMOS and SMAP products (Lievens et al. 2015; Miernecki et al.

776 2014), which both provide an accuracy of 0.04 m^3 m^{-3} (Zhang et al. 2019). However, the actual

777 observation error of these two products typically depends on the spatial location and time of the year

778 (RMSD varying between 0.035 and 0.056 m^3 m^{-3} for several retrieval configurations) (Brocca et al. 2012).

779 According to Purdy et al. (2018), the ET simulated by PT-JPL$_{SM}$ using the 9 km SM_L3_P_E data showed

780 an inferior agreement (R^2= 0.47) but a relatively low RMSD (0.77 mm d^{-1}), due to the SMAP errors in

781 the grid cell with soil heterogeneity and the climatological differences between model SM forecasts and

782 SMAP SSM (Reichle and Koster 2004). We rescaled the ET$_{PM}$ to the probability distribution of the ET$_{LPJ}$

783 through a cumulative distribution function (CDF) to correct the potential seasonal biases of ET$_{PM}$ before

784 assimilation.

Second, there is large uncertainty in the influence of ~~root zone SM~~RZSM as the source of water available to plants (Albergel et al. 2008; Bonan et al. 2020). Our GPP results of irrigated sites~~cropland sites~~ were largely influenced by US-Ne1, an irrigate site. This site maintained high annual GPP in 2012 despite the drought (Figure ~~S4~~S8). However, the SMOS SSM in 2012 had a lower ~~surface~~ SSM annual mean than the site observations likely because the detected soil layer (0-50 cm) of the site observation is deeper than that of the satellite retrieval and the cumulative deep soil moisture due to the regular irrigation was higher than the ~~surface~~ SSM that could easily be vaporized during the drought period (Figure ~~S4~~S8). Therefore, the influence of deep SM of some cropland sites during the drought years induced large simulation errors and unsatisfactory assimilation performance. Moreover, some deep-rooted forests maintain a high LAI during drought by absorbing deep SM (>2 m) and groundwater (Zhang et al. 2016). Thus, joint assimilation of the LAI and SSM may eliminate a portion of the underestimation of GPP of such vegetation in drought periods. Therefore, further research is needed on how to optimally utilize satellite SM data for improving GPP and ET simulations.

Third, the problem of mixed pixels and mismatches in the observation footprints may also have an influence on the accuracy of estimated GPP and ET. The 5 km spatial resolution of the GLASS LAI ,9 km of SMAP, and 25 km of SMOS products cannot capture the sub-grid-scale condition, especially in grid cells for complex land surfaces or strong soil heterogeneity. To ensure the consistency of the grid-cell representativeness for the LAI and SSM, the interpolation result in errors that propagate through the modeling and assimilation, causing the accumulation of output errors (Nijssen and Lettenmaier 2004). Moreover, the shrubland in the LPJ-DGVM was most likely simulated as C4 grassland in the

hydrothermal condition of semi-arid and arid regions. In contrast, the shrubland tended to be hybrid vegetation types (grassland mixed with other types of forest vegetation) in the hydrothermal condition of humid and sub-dry humid regions, and the simulated canopy height is closer to the real condition of shrubland. This might also be the reason for the superior performance of ET_{LPJ} and assimilation results of shrubland sites in humid and sub-dry humid regions.

When assimilating multiple data streams, all data streams could be in the same optimization (simultaneous assimilation) or use a sequential (step-by-step) approach. Mathematically, simultaneous optimization is optimal because strong parametric connections are maintained between different processes. However, complications may arise due to computational constraints related to the inversion of large matrices or the requirement of numerous simulations, particularly for global datasets (e.g. Peylin et al.,2016), and due to the "weight" of different data streams in the optimization (e.g. Wutzler and Carvalhais, 2014). This is particularly true when considering a regional-to-global-scale, multiple site optimization of a complex model that contains many parameters, and which typically takes on the order of minutes to an hour to run a one-year simulation. In practice, it is very difficult to define a probability distribution that properly characterizes the model structural uncertainty and observation errors accounting for biases and non-Gaussian distributions. Nevertheless, a step-wise assimilation may be useful in dealing with possible inconsistencies on a temporary basis, since parameter error covariance matrix must be propagated at each step. It's worth noting that the deviation between the model and observational data should be solved in the process of step-wise assimilation, such as the joint assimilation in this study, the satellite observations and model simulation were fitting through the CDF method so that the first step

825 assimilation will strongly constrain the uncertainty of parameters related to phenology and carbon flux

826 and propagate to the second step . Alternative solutions were found for water -related parameters through

827 soil moisture, providing a better fit for all data streams.   The sequence of assimilation is essential in the

828 step-wise assimilation, and if the first observation contains a strong BIASbias, then the associated error

829 correlation will also propagate through the first assimilation. If the autocorrelation in the observation error,

830 or the correlation between the data stream errors is not considered, it is likely that the posterior simulation

831 has been overturned. That is, we overestimate the reduction in parametric uncertainty. If two observational

832 data are less uncertainty (i.e., high precision of observation data), and the model of deviation is smaller

833 (depend on the spatial scale and inversion method). Moreover, the correlation of these observations is

834 stronger, and contain enough spatio-temporal information to limit all the parameters optimization

835 accurately, the step-wise assimilation performance is basically the same as that of simultaneous

836 assimilation.

837 **6. Conclusions**

838   We developed an assimilation system LPJ-VSJA that integrates GLASS LAI, SMOS SSM, and

839 SMAP SSM data to improve GPP and ET estimates globally. The system was designed to assimilate two

840 SSM products (SMOS and SMAP) into the integrated model - LPJ-PM for both dry and humid regions

841 through separate and joint assimilation. The results show that the joint constraints provided by vegetation

842 and soil variable strategies improve model simulations. Both the original and joint assimilation results for

843 GPP and ET in semi-arid and arid regions performed better than those in humid and dry-subsub-dry humid

844 regions, and the LPJ-PM that emphasized the SSM information is more suitable for the water-limited

845 regions. For ET assimilation, the different SSM products influence assimilation performance, and SMAP

846 SSM possesses a slight advantage in most vegetation types and in both dry and humid regions. Our global

847 LPJ-VSJA GPP and ET products have relatively higher accuracy than other products, especially in water-

848 limited regions with lower ET values.

Data availability

850 The LPJ-DGVM v4.1 version code (LPJ-ML) and example configurations are public available via the

851 project homepage (https://github.com/PIK-LPJmL/LPJmL). We used the 3.01 version of LPJ-DGVM,

852 which removed the agricultural management module. The access of all the input and validation dataset of

853 assimilation system have been described in article. The assimilation method code configured by Fortran

854 platform could be provided by contacting the X.T co-author. The modified code of LPJ-PM model and

855 the underlying and global LPJ-VSJA GPP and ET data can be obtained by contacting the lead author of

856 this manuscript.

Author contributions

858 S.L. and L.Z. designed the experiment and wrote the paper with support from all coauthors. S.L. and R.M.

859 implemented the codes necessary for the experiments. J.X. contributed to the structure of the article and

860 comparison of assimilation performance between the SMOS and SMAP experiments. X.T provided the

861 POD-En4DVAR method and the code. M.Y contributed to the validation and analysis of the results. All

862 the authors contributed to the synthesis of results and key conclusions.

Competing interests

The authors declare that they have no known competing financial interests or personal relationships that could have appeared to influence the work reported in this paper.

Financial support

S.L., L.Z., R.M., and M.Y. were funded by the National Natural Science Foundation of China (Grant No. 41771392; PI Li Zhang) and (Grant No. 41901364; PI Min Yan).

References

Albergel, C., Rüdiger, C., Pellarin, T., Calvet, J.-C., Fritz, N., Froissard, F., Suquia, D., Petitpa, A., Piguet, B., & Martin, E. (2008). From near-surface to root-zone soil moisture using an exponential filter: an assessment of the method based on in-situ observations and model simulations. *Hydrology and Earth System Sciences, 12*, 1323-1337

Albergel, C., Calvet, J.-C., Mahfouf, J.-F., Rüdiger, C., Barbu, A. L., Lafont, S., Roujean, J.-L., Walker, J. P., Crapeau, M., and Wigneron, J.-P.: Monitoring of water and carbon fluxes using a land data assimilation system: a case study for southwestern France, Hydrol. Earth Syst. Sci., 14, 1109–1124, https://doi.org/10.5194/hess-14-1109-2010, 2010.

Albergel, C., Zheng, Y., Bonan, B., Dutra, E., Rodríguez-Fernández, N., Munier, S., Draper, C., de Rosnay, P., Muñoz-Sabater, J., Balsamo, G., Fairbairn, D., Meurey, C., and Calvet, J.-C.: Data assimilation for continuous global assessment of severe conditions over terrestrial surfaces, Hydrol. Earth Syst. Sci., 24, 4291–4316, https://doi.org/10.5194/hess-24-4291-2020, 2020.

Anav, A., Friedlingstein, P., Beer, C., Ciais, P., Harper, A., Jones, C., Murray‐Tortarolo, G., Papale, D., Parazoo, N.C., & Peylin, P. (2015). Spatiotemporal patterns of terrestrial gross primary production: A review. *Reviews of Geophysics, 53*, 785-818

Barth, A., Beckers, J. M., Troupin, C., Alvera-Azcárate, A., & Vandenbulcke, L. (2014). divand-1.0: n-dimensional variational data analysis for ocean observations. Geoscientific Model Development, 7, 225-241Bateni, S.M., Entekhabi, D., Margulis, S., Castelli, F., Kergoat, L., 2014. Coupled estimation of surface heat fluxes and vegetation dynamics from remotely sensed land surface temperature and fraction of photosynthetically active radiation. Water Resour. Res. 50, 8420–8440. https://doi.org/10.1002/2013WR014573

Blyverket, J., Hamer, P.D., Bertino, L., Albergel, C., Fairbairn, D., & Lahoz, W.A. (2019). An Evaluation of the EnKF vs. EnOI and the Assimilation of SMAP, SMOS and ESA CCI Soil Moisture Data over the Contiguous US. *Remote Sensing, 11*, 478

Bonan, B., Albergel, C., Zheng, Y., Barbu, A.L., Fairbairn, D., Munier, S., & Calvet, J.-C. (2020). An ensemble square root filter for the joint assimilation of surface soil moisture and leaf area index within the Land Data Assimilation System LDAS-Monde: application over the Euro-Mediterranean region. *Hydrology and Earth System Sciences, 24*, 325-347

Bonan, G., Williams, M., Fisher, R., & Oleson, K. (2014). Modeling stomatal conductance in the earth system: linking leaf water-use efficiency and water transport along the soil–plant–atmosphere continuum. *Geoscientific Model Development, 7*, 2193-2222

Brocca, L., Tullo, T., Melone, F., Moramarco, T., & Morbidelli, R. (2012). Catchment scale soil moisture spatial–temporal variability. *Journal of hydrology, 422*, 63-75

Burgin, M.S., Colliander, A., Njoku, E.G., Chan, S.K., Cabot, F., Kerr, Y.H., Bindlish, R., Jackson, T.J., Entekhabi, D., & Yueh, S.H. (2017). A comparative study of the SMAP passive soil moisture product with existing satellite-based soil moisture products. *IEEE Transactions on Geoscience and Remote Sensing, 55*, 2959-2971

Caires, S., & Sterl, A. (2003). Validation of ocean wind and wave data using triple collocation. *Journal of geophysical research: oceans, 108*

Chan, S.K., Bindlish, R., O'Neill, P.E., Njoku, E., Jackson, T., Colliander, A., Chen, F., Burgin, M., Dunbar, S., & Piepmeier, J. (2016). Assessment of the SMAP passive soil moisture product. *IEEE Transactions on Geoscience and Remote Sensing, 54*, 4994-5007

Cui, C., Xu, J., Zeng, J., Chen, K.-S., Bai, X., Lu, H., Chen, Q., & Zhao, T. (2018). Soil moisture mapping from satellites: An intercomparison of SMAP, SMOS, FY3B, AMSR2, and ESA CCI over two dense network regions at different spatial scales. *Remote Sensing, 10*, 33

Desai, A.R., Moore, D.J., Ahue, W.K., Wilkes, P.T., De Wekker, S.F., Brooks, B.G., Campos, T.L., Stephens, B.B., Monson, R.K., & Burns, S.P. (2011). Seasonal pattern of regional carbon balance in the central Rocky Mountains from surface and airborne measurements. *Journal of Geophysical Research: Biogeosciences, 116*

Draper, C., Mahfouf, J.-F., Calvet, J.-C., Martin, E., & Wagner, W. (2011). Assimilation of ASCAT near-surface soil moisture into the SIM hydrological model over France. *Hydrology and Earth System Sciences, 15*, 3829-3841

Entekhabi, D., Njoku, E.G., O'Neill, P.E., Kellogg, K.H., Crow, W.T., Edelstein, W.N., Entin, J.K., Goodman, S.D., Jackson, T.J., & Johnson, J. (2010). The soil moisture active passive (SMAP) mission. *Proceedings of the IEEE, 98*, 704-716

Etheridge, D.M., Steele, L., Langenfelds, R.L., Francey, R.J., Barnola, J.M., & Morgan, V. (1996). Natural and anthropogenic changes in atmospheric CO2 over the last 1000 years from air in Antarctic ice and firn. *Journal of Geophysical Research: Atmospheres, 101*, 4115-4128

Evensen, G. (2004). Sampling strategies and square root analysis schemes for the EnKF. *Ocean dynamics, 54*, 539-560

Exbrayat, JF., Bloom, A.A., Carvalhais, N. et al. Understanding the Land Carbon Cycle with Space Data: Current Status and Prospects. Surv Geophys 40, 735–755 (2019). https://doi.org/10.1007/s10712-019-09506-2

Fang, H., Baret, F., Plummer, S., & Schaepman‐Strub, G. (2019). An overview of global leaf area index (LAI): Methods, products, validation, and applications. *Reviews of Geophysics, 57*, 739-799

Fang, H., Beaudoing, H.K., Rodell, M., Teng, W.L., & Vollmer, B.E. (2009). Global Land data assimilation system (GLDAS) products, services and application from NASA hydrology data and information services center (HDISC). In, *ASPRS 2009 Annual Conference, Baltimore, Maryland* (pp. 8-13)

Fang, H., & Liang, S. (2005). A hybrid inversion method for mapping leaf area index from MODIS data: Experiments and application to broadleaf and needleleaf canopies. *Remote Sensing of Environment, 94*, 405-424

Feng, F., Chen, J., Li, X., Yao, Y., Liang, S., Liu, M., Zhang, N., Guo, Y., Yu, J., & Sun, M. (2015). Validity of five satellite-based latent heat flux algorithms for semi-arid ecosystems. *Remote Sensing, 7*, 16733-16755

Friedl, M.A., Sulla-Menashe, D., Tan, B., Schneider, A., Ramankutty, N., Sibley, A., & Huang, X. (2010). MODIS Collection 5 global land cover: Algorithm refinements and characterization of new datasets. *Remote Sensing of Environment, 114*, 168-182

Gokmen, M., Vekerdy, Z., Verhoef, A., Verhoef, W., Batelaan, O., & Van der Tol, C. (2012). Integration of soil moisture in SEBS for improving evapotranspiration estimation under water stress conditions. *Remote Sensing of Environment, 121*, 261-274

Gonsamo, A., & Chen, J.M. (2011). Evaluation of the GLC2000 and NALC2005 land cover products for LAI retrieval over Canada. *Canadian Journal of Remote Sensing, 37*, 302-313

Haxeltine, A., & Prentice, I.C. (1996). BIOME3: An equilibrium terrestrial biosphere model based on ecophysiological constraints, resource availability, and competition among plant functional types. *Global biogeochemical cycles, 10*, 693-709

Hayes, D.J., Turner, D.P., Stinson, G., McGuire, A.D., Wei, Y., West, T.O., Heath, L.S., De Jong, B., McConkey, B.G., & Birdsey, R.A. (2012). Reconciling estimates of the contemporary North American carbon balance among terrestrial biosphere models, atmospheric inversions, and a new approach for estimating net ecosystem exchange from inventory‐based data. *Global Change Biology, 18*, 1282-1299

He, L., Chen, J.M., Liu, J., Bélair, S., & Luo, X. (2017). Assessment of SMAP soil moisture for global simulation of gross primary production. *Journal of Geophysical Research: Biogeosciences, 122*, 1549-1563

He, Xinlei, Xu, T., Bateni, S.M., Ki, S.J., Xiao, J., Liu, S., Song, L., He, Xiangping, 2021. Estimation of Turbulent Heat Fluxes and Gross Primary Productivity by Assimilating Land Surface Temperature and Leaf Area Index. Water Res 57. https://doi.org/10.1029/2020WR028224

Huang, C., Li, Y., Gu, J., Lu, L., & Li, X. (2015). Improving estimation of evapotranspiration under water-limited conditions based on SEBS and MODIS data in arid regions. *Remote Sensing, 7*, 16795-16814

Ines, A.V., Das, N.N., Hansen, J.W., & Njoku, E.G. (2013). Assimilation of remotely sensed soil moisture and vegetation with a crop simulation model for maize yield prediction. *Remote Sensing of Environment, 138*, 149-164

Jacquette, E., Al Bitar, A., Mialon, A., Kerr, Y., Quesney, A., Cabot, F., & Richaume, P. (2010). SMOS CATDS level 3 global products over land. In, *Remote Sensing for Agriculture, Ecosystems, and Hydrology XII* (p. 78240K): International Society for Optics and Photonics

Kaminski, T., Scholze, M., Vossbeck, M., Knorr, W., Buchwitz, M., & Reuter, M. (2017). Constraining a terrestrial biosphere model with remotely sensed atmospheric carbon dioxide. *Remote Sensing of Environment, 203*, 109-124

Kato, T., Knorr, W., Scholze, M., Veenendaal, E., Kaminski, T., Kattge, J., & Gobron, N. (2013). Simultaneous assimilation of satellite and eddy covariance data for improving terrestrial water and carbon simulations at a semi-arid woodland site in Botswana. *Biogeosciences, 10*, 789-802

Keeling, C.D., Whorf, T.P., Wahlen, M., & Van der Plichtt, J. (1995). Interannual extremes in the rate of rise of atmospheric carbon dioxide since 1980. *Nature, 375*, 666-670

Keller, M., Schimel, D.S., Hargrove, W.W., & Hoffman, F.M. (2008). A continental strategy for the National Ecological Observatory Network. *Frontiers in Ecology and the Environment, 6*, 282-284

Kganyago, M., Mhangara, P., Alexandridis, T., Laneve, G., Ovakoglou, G., & Mashiyi, N. (2020). Validation of sentinel-2 leaf area index (LAI) product derived from SNAP toolbox and its comparison with global LAI products in an African semi-arid agricultural landscape. *Remote Sensing Letters, 11*, 883-892

Khan, M.S., Liaqat, U.W., Baik, J., & Choi, M. (2018). Stand-alone uncertainty characterization of GLEAM, GLDAS and MOD16 evapotranspiration products using an extended triple collocation approach. *Agricultural and Forest Meteorology, 252*, 256-268

Kim, H., Parinussa, R., Konings, A.G., Wagner, W., Cosh, M.H., Lakshmi, V., Zohaib, M., & Choi, M. (2018). Global-scale assessment and combination of SMAP with ASCAT (active) and AMSR2 (passive) soil moisture products. *Remote Sensing of Environment, 204*, 260-275

Koster, R.D., Crow, W.T., Reichle, R.H., & Mahanama, S.P. (2018). Estimating basin‐scale water budgets with SMAP soil moisture data. *Water resources research, 54*, 4228-4244

Law, B., Falge, E., Gu, L.v., Baldocchi, D., Bakwin, P., Berbigier, P., Davis, K., Dolman, A., Falk, M., & Fuentes, J. (2002). Environmental controls over carbon dioxide and water vapor exchange of terrestrial vegetation. *Agricultural and Forest Meteorology, 113*, 97-120

Lee, H., Seo, D.-J., & Koren, V. (2011). Assimilation of streamflow and in situ soil moisture data into operational distributed hydrologic models: Effects of uncertainties in the data and initial model soil moisture states. *Advances in water resources, 34*, 1597-1615

Li, B., & Rodell, M. (2013). Spatial variability and its scale dependency of observed and modeled soil moisture over different climate regions. *Hydrology and Earth System Sciences, 17*, 1177-1188

Li C, Tang G, Hong Y. Cross-evaluation of ground-based, multi-satellite and reanalysis precipitation products: Applicability of the Triple Collocation method across Mainland China[J]. Journal of Hydrology, 2018, 562: 71-83.

Li, S., Wang, G., Sun, S., Chen, H., Bai, P., Zhou, S., Huang, Y., Wang, J., & Deng, P. (2018). Assessment of multi-source evapotranspiration products over china using eddy covariance observations. *Remote Sensing, 10*, 1692

Li, S., Zhang, L., Ma, R., Yan, M., & Tian, X. (2020). Improved ET assimilation through incorporating SMAP soil moisture observations using a coupled process model: A study of US arid and semiarid regions. *Journal of hydrology, 590*, 125402

Li, X., Cheng, G., Liu, S., Xiao, Q., Ma, M., Jin, R., Che, T., Liu, Q., Wang, W., & Qi, Y. (2013). Heihe watershed allied telemetry experimental research (HiWATER): Scientific objectives and experimental design. *Bulletin of the American Meteorological Society, 94*, 1145-1160

Li, X., Mao, F., Du, H., Zhou, G., Xu, X., Han, N., Sun, S., Gao, G., & Chen, L. (2017). Assimilating leaf area index of three typical types of subtropical forest in China from MODIS time series data based on the integrated ensemble Kalman filter and PROSAIL model. *ISPRS Journal of Photogrammetry and Remote Sensing, 126*, 68-78

Li, X., & Xiao, J. (2019). A global, 0.05-degree product of solar-induced chlorophyll fluorescence derived from OCO-2, MODIS, and reanalysis data. *Remote Sensing, 11*, 517

Liang, S., Zhao, X., Liu, S., Yuan, W., Cheng, X., Xiao, Z., Zhang, X., Liu, Q., Cheng, J., & Tang, H. (2013). A long-term Global LAnd Surface Satellite (GLASS) data-set for environmental studies. *International Journal of Digital Earth, 6*, 5-33

Lievens, H., Tomer, S.K., Al Bitar, A., De Lannoy, G.J., Drusch, M., Dumedah, G., Franssen, H.-J.H., Kerr, Y.H., Martens, B., & Pan, M. (2015). SMOS soil moisture assimilation for improved hydrologic simulation in the Murray Darling Basin, Australia. *Remote Sensing of Environment, 168*, 146-162

Ling, X.-L., Fu, C.-B., Yang, Z.-L., & Guo, W.-D. (2019). Comparison of different sequential assimilation algorithms for satellite-derived leaf area index using the Data Assimilation Research Testbed (version Lanai). *Geoscientific Model Development, 12*, 3119-3133

Liu, L., Gudmundsson, L., Hauser, M., Qin, D., Li, S., & Seneviratne, S.I. (2020). Soil moisture dominates dryness stress on ecosystem production globally. *Nature communications, 11*, 1-9

Liu, Y., Xiao, J., Ju, W., Zhu, G., Wu, X., Fan, W., Li, D., & Zhou, Y. (2018). Satellite-derived LAI products exhibit large discrepancies and can lead to substantial uncertainty in simulated carbon and water fluxes. *Remote Sensing of Environment, 206*, 174-188

Ma, H., Huang, J., Zhu, D., Liu, J., Su, W., Zhang, C., & Fan, J. (2013). Estimating regional winter wheat yield by assimilation of time series of HJ-1 CCD NDVI into WOFOST–ACRM model with Ensemble Kalman Filter. *Mathematical and Computer Modelling, 58*, 759-770

Ma, R., Zhang, L., Tian, X., Zhang, J., Yuan, W., Zheng, Y., Zhao, X., & Kato, T. (2017). Assimilation of remotely-sensed leaf area index into a dynamic vegetation model for gross primary productivity estimation. *Remote Sensing, 9*, 188

MacBean, N., Peylin, P., Chevallier, F., Scholze, M., & Schürmann, G. (2016). Consistent assimilation of multiple data streams in a carbon cycle data assimilation system. *Geoscientific Model Development, 9*, 3569-3588

Martens, B., Miralles, D.G., Lievens, H., Schalie, R.v.d., De Jeu, R.A., Fernández-Prieto, D., Beck, H.E., Dorigo, W.A., & Verhoest, N.E. (2017). GLEAM v3: Satellite-based land evaporation and root-zone soil moisture. *Geoscientific Model Development, 10*, 1903-1925

Miernecki, M., Wigneron, J.-P., Lopez-Baeza, E., Kerr, Y., De Jeu, R., De Lannoy, G.J., Jackson, T.J., O'Neill, P.E., Schwank, M., & Moran, R.F. (2014). Comparison of SMOS and SMAP soil moisture retrieval approaches using tower-based radiometer data over a vineyard field. *Remote Sensing of Environment, 154*, 89-101

Miralles, D.G., Jiménez, C., Jung, M., Michel, D., Ershadi, A., McCabe, M., Hirschi, M., Martens, B., Dolman, A.J., & Fisher, J.B. (2016). The WACMOS-ET project–Part 2: Evaluation of global terrestrial evaporation data sets. *Hydrology and Earth System Sciences, 20*, 823-842

Mitchell, H.L., Houtekamer, P.L., & Pellerin, G. (2002). Ensemble size, balance, and model-error representation in an ensemble Kalman filter. *Monthly weather review, 130*, 2791-2808

Mu, Q., Zhao, M., Heinsch, F.A., Liu, M., Tian, H., & Running, S.W. (2007). Evaluating water stress controls on primary production in biogeochemical and remote sensing based models. *Journal of Geophysical Research: Biogeosciences, 112*

New, M., Hulme, M., & Jones, P. (2000). Representing twentieth-century space–time climate variability. Part II: Development of 1901–96 monthly grids of terrestrial surface climate. *Journal of climate, 13*, 2217-2238

Nijssen, B., & Lettenmaier, D.P. (2004). Effect of precipitation sampling error on simulated hydrological fluxes and states: Anticipating the Global Precipitation Measurement satellites. *Journal of Geophysical Research: Atmospheres, 109*

O'Neill, P., Entekhabi, D., Njoku, E., & Kellogg, K. (2010). The NASA soil moisture active passive (SMAP) mission: Overview. In, *2010 IEEE International Geoscience and Remote Sensing Symposium* (pp. 3236-3239): IEEE

O'Carroll, A.G., Eyre, J.R., & Saunders, R.W. (2008). Three-way error analysis between AATSR, AMSR-E, and in situ sea surface temperature observations. *Journal of atmospheric and oceanic technology, 25*, 1197-1207

Pan, H.; Chen, Z.; de Wit, A.; Ren, J. Joint Assimilation of Leaf Area Index and Soil Moisture from Sentinel-1 and Sentinel-2 Data into the WOFOST Model for Winter Wheat Yield Estimation. Sensors 2019, 19, 3161.

Pardo, N., Sánchez, M.L., Timmermans, J., Su, Z., Pérez, I.A., & García, M.A. (2014). SEBS validation in a Spanish rotating crop. *Agricultural and Forest Meteorology, 195*, 132-142

Petropoulos, G.P., Ireland, G., & Barrett, B. (2015). Surface soil moisture retrievals from remote sensing: Current status, products & future trends. *Physics and Chemistry of the Earth, Parts A/B/C, 83*, 36-56

Pipunic, R., Walker, J., & Western, A. (2008). Assimilation of remotely sensed data for improved latent and sensible heat flux prediction: A comparative synthetic study. *Remote Sensing of Environment, 112*, 1295-1305

Purdy, A.J., Fisher, J.B., Goulden, M.L., Colliander, A., Halverson, G., Tu, K., & Famiglietti, J.S. (2018). SMAP soil moisture improves global evapotranspiration. *Remote Sensing of Environment, 219*, 1-14

Rahman, A., Zhang, X., Houser, P., Sauer, T., Maggioni, V., 2022. Global Assimilation of Remotely Sensed Leaf Area Index: The Impact of Updating More State Variables Within a Land Surface Model. Front. Water 3, 789352. https://doi.org/10.3389/frwa.2021.789352

Rahman, A.; Maggioni, V.; Zhang, X.; Houser, P.; Sauer, T.; Mocko, D.M. The Joint Assimilation of Remotely Sensed Leaf Area Index and Surface Soil Moisture into a Land Surface Model. Remote Sens. 2022, 14, 437. https://doi.org/10.3390/rs14030437

Rüdiger, C., Albergel, C., Mahfouf, J.F., Calvet, J.C., & Walker, J.P. (2010). Evaluation of the observation operator Jacobian for leaf area index data assimilation with an extended Kalman filter. *Journal of Geophysical Research: Atmospheres, 115*Reichle, R.H., De Lannoy, G.J., Liu, Q., Koster, R.D., Kimball, J.S., Crow, W.T., Ardizzone, J.V., Chakraborty, P., Collins, D.W., & Conaty, A.L. (2017). Global assessment of the SMAP level-4 surface and root-zone soil moisture product using assimilation diagnostics. *Journal of Hydrometeorology, 18*, 3217-3237

Reichle, R.H., & Koster, R.D. (2004). Bias reduction in short records of satellite soil moisture. *Geophysical Research Letters, 31*

Rienecker, M.M., Suarez, M.J., Gelaro, R., Todling, R., Bacmeister, J., Liu, E., Bosilovich, M.G., Schubert, S.D., Takacs, L., & Kim, G.-K. (2011). MERRA: NASA's modern-era retrospective analysis for research and applications. *Journal of climate, 24*, 3624-3648

Running, S.W., Nemani, R.R., Heinsch, F.A., Zhao, M., Reeves, M., & Hashimoto, H. (2004). A continuous satellite-derived measure of global terrestrial primary production. *Bioscience, 54*, 547-560

Scholze, M., Buchwitz, M., Dorigo, W., Guanter, L., and Quegan, S.: Reviews and syntheses: Systematic Earth observations for use in terrestrial carbon cycle data assimilation systems, Biogeosciences, 14, 3401–3429, https://doi.org/10.5194/bg-14-3401-2017, 2017.

Seneviratne, S.I., Corti, T., Davin, E.L., Hirschi, M., Jaeger, E.B., Lehner, I., Orlowsky, B., & Teuling, A.J. (2010). Investigating soil moisture–climate interactions in a changing climate: A review. *Earth-Science Reviews, 99*, 125-161

Sitch, S., Smith, B., Prentice, I.C., Arneth, A., Bondeau, A., Cramer, W., Kaplan, J.O., Levis, S., Lucht, W., & Sykes, M.T. (2003). Evaluation of ecosystem dynamics, plant geography and terrestrial carbon cycling in the LPJ dynamic global vegetation model. *Global Change Biology, 9*, 161-185

Stoffelen, A. (1998). Toward the true near‐surface wind speed: Error modeling and calibration using triple collocation. *Journal of geophysical research: oceans, 103*, 7755-7766

Sun, P., Wu, Y., Xiao, J., Hui, J., Hu, J., Zhao, F., Qiu, L., & Liu, S. (2019). Remote sensing and modeling fusion for investigating the ecosystem water-carbon coupling processes. *Science of the total environment, 697*, 134064

Taylor, K.E. (2001). Summarizing multiple aspects of model performance in a single diagram. *Journal of Geophysical Research: Atmospheres, 106*, 7183-7192

Tian, S., Renzullo, L.J., Van Dijk, A.I., Tregoning, P., & Walker, J.P. (2019). Global joint assimilation of GRACE and SMOS for improved estimation of root-zone soil moisture and vegetation response. *Hydrology and Earth System Sciences, 23*, 1067-1081

Tian, X., & Feng, X. (2015). A non-linear least squares enhanced POD-4DVar algorithm for data assimilation. *Tellus A: Dynamic Meteorology and Oceanography, 67*, 25340

Tian, X., Xie, Z., Dai, A., Jia, B., & Shi, C. (2010). A microwave land data assimilation system: Scheme and preliminary evaluation over China. *Journal of Geophysical Research: Atmospheres, 115*

Tian, X., Xie, Z., Dai, A., Shi, C., Jia, B., Chen, F., & Yang, K. (2009). A dual‐pass variational data assimilation framework for estimating soil moisture profiles from AMSR‐E microwave brightness temperature. *Journal of Geophysical Research: Atmospheres, 114*

Tian, X., Xie, Z., Liu, Y., Cai, Z., Fu, Y., Zhang, H., & Feng, L. (2014). A joint data assimilation system (Tan-Tracker) to simultaneously estimate surface CO_2 fluxes and 3-D atmospheric CO_2 concentrations from observations. *Atmospheric Chemistry and Physics, 14*, 13281-13293

Tian, X., Xie, Z., & Sun, Q. (2011). A POD-based ensemble four-dimensional variational assimilation method. *Tellus A: Dynamic Meteorology and Oceanography, 63*, 805-816

Twine, T.E., Kustas, W., Norman, J., Cook, D., Houser, P., Meyers, T., Prueger, J., Starks, P., & Wesely, M. (2000). Correcting eddy-covariance flux underestimates over a grassland. *Agricultural and Forest Meteorology, 103*, 279-300

Wang, L., Zhu, H., Lin, A., Zou, L., Qin, W., & Du, Q. (2017). Evaluation of the latest MODIS GPP products across multiple biomes using global eddy covariance flux data. *Remote Sensing, 9*, 418

Waring, R.H., & Running, S.W. (2010). *Forest ecosystems: analysis at multiple scales*. Elsevier

Wieder, W., Boehnert, J., Bonan, G., & Langseth, M. (2014). Regridded harmonized world soil database v1. 2. *ORNL DAAC*

Wu, M.; Scholze, M.; Voßbeck, M.; Kaminski, T.; Hoffmann, G. Simultaneous Assimilation of Remotely Sensed Soil Moisture and FAPAR for Improving Terrestrial Carbon Fluxes at Multiple Sites Using CCDAS. Remote Sens. 2019, 11, 27. https://doi.org/10.3390/rs11010027

Xiao, J., Chevallier, F., Gomez, C., Guanter, L., Hicke, J.A., Huete, A.R., Ichii, K., Ni, W., Pang, Y., & Rahman, A.F. (2019). Remote sensing of the terrestrial carbon cycle: A review of advances over 50 years. *Remote Sensing of Environment, 233*, 111383

Xiao, Z., Liang, S., & Jiang, B. (2017). Evaluation of four long time-series global leaf area index products. *Agricultural and Forest Meteorology, 246*, 218-230

Xiao, Z., Liang, S., Wang, J., Chen, P., Yin, X., Zhang, L., & Song, J. (2013). Use of general regression neural networks for generating the GLASS leaf area index product from time-series MODIS surface reflectance. *IEEE Transactions on Geoscience and Remote Sensing, 52*, 209-223

Xiao, Z., Liang, S., Wang, J., Xiang, Y., Zhao, X., & Song, J. (2016). Long-time-series global land surface satellite leaf area index product derived from MODIS and AVHRR surface reflectance. *IEEE Transactions on Geoscience and Remote Sensing, 54*, 5301-5318

Xie, Y.; Wang, P.; Sun, H.; Zhang, S.; Li, L. Assimilation of Leaf Area Index and Surface Soil Moisture With the CERES-Wheat Model for Winter Wheat Yield Estimation Using a Particle Filter Algorithm. IEEE J. Sel. Top. Appl. Earth Obs. Remote Sens. 2017, 10, 1303–1316.

Xu, T., He, X., Bateni, S.M., Auligne, T., Liu, S., Xu, Z., Zhou, J., Mao, K., 2019. Mapping regional turbulent heat fluxes via variational assimilation of land surface temperature data from polar orbiting satellites. Remote Sensing of Environment 221, 444–461. https://doi.org/10.1016/j.rse.2018.11.023

Xu, T., Chen, F., He, Xinlei, Barlage, M., Zhang, Z., Liu, S., He, Xiangping, 2021. Improve the Performance of the Noah-MP-Crop Model by Jointly Assimilating Soil Moisture and Vegetation Phenology Data. J Adv Model Earth Syst 13. https://doi.org/10.1029/2020MS002394

Yan, M., Tian, X., Li, Z., Chen, E., Wang, X., Han, Z., & Sun, H. (2016). Simulation of forest carbon fluxes using model incorporation and data assimilation. *Remote Sensing, 8*, 567

Yang, W., Wang, Y., Liu, X., Zhao, H., Shao, R., & Wang, G. (2020). Evaluation of the rescaled complementary principle in the estimation of evaporation on the Tibetan Plateau. *Science of the total environment, 699*, 134367

Yang, X., Yong, B., Ren, L., Zhang, Y., & Long, D. (2017). Multi-scale validation of GLEAM evapotranspiration products over China via ChinaFLUX ET measurements. *International Journal of Remote Sensing, 38*, 5688-5709

Yilmaz, M.T., & Crow, W.T. (2014). Evaluation of assumptions in soil moisture triple collocation analysis. *Journal of Hydrometeorology, 15*, 1293-1302

Yuan, W., Liu, S., Yu, G., Bonnefond, J.-M., Chen, J., Davis, K., Desai, A.R., Goldstein, A.H., Gianelle, D., & Rossi, F. (2010). Global estimates of evapotranspiration and gross primary production based on MODIS and global meteorology data. *Remote Sensing of Environment, 114*, 1416-1431

Zhang, D.-H., Li, X.-R., Zhang, F., Zhang, Z.-S., & Chen, Y.-L. (2016). Effects of rainfall intensity and intermittency on woody vegetation cover and deep soil moisture in dryland ecosystems. *Journal of hydrology, 543*, 270-282

Zhang, F., & Weng, Y. (2015). Predicting hurricane intensity and associated hazards: A five-year real-time forecast experiment with assimilation of airborne Doppler radar observations. *Bulletin of the American Meteorological Society, 96*, 25-33

Zhang, L., Xiao, J., Zheng, Y., Li, S., & Zhou, Y. (2020). Increased carbon uptake and water use efficiency in global semi-arid ecosystems. *Environmental Research Letters, 15*, 034022

Zhang, X., Huang, X.-Y., Liu, J., Poterjoy, J., Weng, Y., Zhang, F., & Wang, H. (2014). Development of an efficient regional four-dimensional variational data assimilation system for WRF. Journal of atmospheric and oceanic technology, 31, 2777-2794

Zhang, R., Kim, S., & Sharma, A. (2019). A comprehensive validation of the SMAP Enhanced Level-3 Soil Moisture product using ground measurements over varied climates and landscapes. *Remote Sensing of Environment, 223*, 82-94

Zhao, L., Xia, J., Xu, C.-y., Wang, Z., Sobkowiak, L., & Long, C. (2013). Evapotranspiration estimation methods in hydrological models. *Journal of Geographical Sciences, 23*, 359-369

Zobitz, J., Moore, D.J., Quaife, T., Braswell, B.H., Bergeson, A., Anthony, J.A., & Monson, R.K. (2014). Joint data assimilation of satellite reflectance and net ecosystem exchange data constrains ecosystem carbon fluxes at a high-elevation subalpine forest. *Agricultural and Forest Meteorology, 195*, 73-88

Zou, L., Zhan, C., Xia, J., Wang, T., & Gippel, C.J. (2017). Implementation of evapotranspiration data assimilation with catchment scale distributed hydrological model via an ensemble Kalman filter. *Journal of hydrology, 549*, 685-702